NTNU
Norwegian University of
Science and Technology

Quantitative Polychromatic X-Ray Computed Tomography

Experiments and Simulations

Kim Robert Bjørk Tekseth

Master of Science in Physics and Mathematics
Submission date: June 2018
Supervisor: Dag Werner Breiby, IFY

Norwegian University of Science and Technology
Department of Physics

Abstract

X-ray Computed Tomography (CT) is an extensively used technique conventionally utilizing either absorption-contrast or phase-contrast to non-destructively image the internal structures of objects. While CT instruments using polychromatic source spectra might provide qualitative information about a sample, quantitative results are limited due to tomographic artifacts such as beam hardening. Beam hardening may be alleviated through energy filtration or using dual energy CT, however, quantitative CT is usually restricted to measurements using a monochromatic source.

This thesis has focused on two dimensional monochromatic and polychromatic CT simulations based on absorption-contrast. The polychromatic simulations aim to replicate a Nikon XT H 225 ST CT instrument by implementing models for the X-ray source and the X-ray detector, the focal spot size and the noise.

Simulated tomograms of three homogeneous and cylindrical samples consisting of polyoxymethylene, polytetrafluoroethylene and Al were compared to experimental data to verify the models used in the simulations. The results indicate that the Poisson noise applied to the simulated projections accurately describes the noise present in the experimental tomograms. Moreover, a larger amount of beam hardening was observed in the simulations compared to the measured tomograms, especially for the high-attenuating sample Al. The discrepancy was arguably due to differences between the real and the simulated source spectra.

A sample consisting of two Si wafers bonded together by a Ni layer and a Ni_3Sn_2 phase layer was further studied. The simulations were performed with a high magnification using a pixel size of 4 μm and a tube voltage of 180 kV. Using a current of 100 μA it was found that the Ni_3Sn_2 layer had to be 64 μm thick in order to be resolved. By decreasing the current to 10 μA the thickness of the Ni_3Sn_2 layer could be resolved at 56 μm, at the expense of increased noise. As the measured focal spot size used in the simulations is larger than the real focal spot size, real CT measurements should have a better physical resolution than presented here.

A sample consisting of a PZT material and a Tungsten Carbide (WC) material bonded together by various Au-Sn phases was measured with a Nikon CT instrument and tomographic images were presented. The presence of beam hardening, ring artifacts and the anode heel effect in the tomograms was discussed.

Lastly, a sample of Si wafers bonded together by Ni-Sn phases was measured at the ID-19 beamline at the European Synchrotron Radiation Facility in Grenoble, France. Due to the partial coherence of the beam giving propagation phase-contrast, the measured projections were preprocessed prior

to reconstruction using the Paganin approximation. However, the tomograms still contained traces of phase-contrast, especially between air and sample materials. It was argued that the constants, δ and β, had been optimized such that the phase contrast in the bond layer was minimized. Inspection of the bond layer revealed the presence of a high attenuating structure and a low attenuating structure. Simulations using monochromatic, incoherent X-rays were compared to the measured tomograms, indicating that the low attenuating structure consisted of Ni with the possibility of a distribution of voids with a micrometer size or smaller. Moreover, it was demonstrated that the high attenuating structure could consist of a Ni_3Sn_2 phase, however, it could not be excluded that other phases could be present in the structure as well. It was argued that more reliable results could be obtained if the phase contrast observed in the measured tomograms could be implemented into the simulations.

Sammendrag

Computertomografi (CT) med røntgenstråler er en utbredt teknikk som anvender absorpsjonskontrast eller fasekontrast til å avbilde innvendige strukturer på en ikke-destruktiv måte. Selv om computertomografi med polykromatisk kilde kan gi kvalitativ informasjon om en prøve, er kvantitative resultater sjeldent oppnåelige på grunn av artefakter som beam hardening. Beam hardening kan reduseres ved å benytte et energifilter eller ved å bruke dual energy CT. Det vil likevel være vanskelig å oppnå kvantitative resultater uten å benytte seg av en monokromatisk kilde.

Denne avhandlingen har fokusert på to-dimensjonale monokromatiske og polykromatiske CT-simuleringer basert på absorpsjonskontrast. Målet med de polykromatiske simuleringene er å etterligne et Nikon XT H 225 ST CT-instrument ved å implementere modeller for strålekilden, stråledetektoren, kildestørrelsen og støy.

Simuleringer av tre homogene, sylindriske prøver bestående av polyoxymetylen, polytetrafluoreten og Al ble sammenlignet med eksperimentelle data for å verifisere modellene som ble brukt i simuleringene. Det ble vist at Poissonfordelt støy pålagt de simulerte projeksjonene beskriver støyen i de eksperimentelle projeksjonene nøyaktig. Videre ble det observert mer beam hardening i de simulerte projeksjonene sammenlignet med de målte projeksjonene, spesielt for Al som har høy attenuasjonsverdi. Det ble argumentert med at forskjellen skyldes forskjeller i den virkelige og den simulerte strålekilden.

En prøve bestående av Si-wafere bundet sammen av et Ni-lag og et Ni_3Sn_2-faselag ble videre studert. Simuleringer ble gjennomført med en pikselstørrelse på 4 μm og en akselerasjonsspenning på 180 kV. Ved å benytte en strøm på 100 μA måtte Ni_3Sn_2-laget være 64 μm tykt for å sikkert skille fasen fra andre faser. Ved å sette strømmen til 10 μA kunne tykkelsen til Ni_3Sn_2-laget reduseres til 56 μm, på bekostning av økt støy. Siden den målte kildestørrelsen er større enn den virkelige kildestørrelsen, vil virkelige CT målinger kunne gi en bedre reell oppløsning enn det som er presentert her.

En prøve bestående av et PZT-materiale og et wolframkarbid-material (WC) bundet sammen av ulike AuSn-faser ble målt med et Nikon CT-instrument og tomografiske bilder ble presentert. Arteftakter som beam hardening, ringartefakter og anode-heel-effekten i tomogrammene ble diskutert.

Avslutningsvis ble en prøve bestående av Si-wafere bundet sammen av Ni-Sn-faser målt ved strålelinje ID-19 ved European Synchrotron Radiation Facility i Grenoble, Frankrike. De målte projeksjonene ble preprosessert med Paganin-approksimasjonen på grunn av den delvis koherente strålekilden som ga propagerende fasekontrast. Tomogrammene inneholdt likevel spor av fasekon-

trast, spesielt mellom luft og prøve. Det ble argumentert for at parametrene δ og β i Paganin-approksimasjonen var optimalisert slik at fasekontrasten i bindelaget var blitt minimert. Ved inspeksjon av bindelaget ble det observert en høy-attenuerende struktur og en lav-attenuerende struktur. Simuleringer med monokromatiske og inkoherente stråler ble sammenlignet med de målte tomogrammene. Resultatene fra simuleringene indikerte at den lav-attenuerende strukturen besto av Ni med flere hull på mikrometerstørrelse eller mindre. Videre ble det vist at den høy-attenuerende fasen kan bestå av Ni_3Sn_2. Det er likevel mulig at andre faser finnes i strukturen. Mer pålitelige resultater når en sammenligner simuleringene med de målte tomogrammene kan oppnås dersom en tar høyde for koherensen til røntgenstrålene.

Preface

The master thesis is the final part of the master's degree programme in *Applied Physics and Mathematics* at Norwegian University of Science and Technology. I have had the pleasure to work with the staff in the condensed matter physics research group of professor Dag Werner Breiby during both my specialization project and my master thesis.

The main work of the master thesis was to develop a tool for simulating the CT instrument at the Department of physics, and was a continuation of the work done in the specialization project during the autumn of 2017. The motivation was to improve and support real CT measurements through simulations. Additional work included an analysis of samples processed through solid-liquid interdiffusion, which were provided by researchers at the University of Southeast Norway.

I would like to thank my supervisor professor Dag Werner Breiby for all his patience, support and guidance during this work. A thank you should also be directed to Ole Tore Buset, an engineer in Breiby's research group, for discussing the working principles of the CT instrument at the Department of physics. I would also like to thank Basab Chattopadhyay for the discussions of the samples from the University of Southeast Norway. Additionally, professor Ragnvald Mathiesen has provided fruitful discussions which I am grateful for.

Furthermore, a thank you should be directed to professor Knut E. Aasmundtveit, Ph. D. student Andreas Larsson and postdoc Hoang Vu Nguyen at the University of Southeast Norway for providing the Au-Sn SLID and the Ni-Sn SLID sample and the related discussions and insights they have provided.

Last, but not least, a thank you must go to Synne Ringen Vannebo for all her support, discussions and proofreading of the thesis during this final semester.

Contents

Chapter 1

Introduction

X-ray Computed Tomography (CT) is a technique used to image the internal structure of objects in a non-invasive and non-destructive manner. Most commonly known is perhaps the use of CT scans in medical imaging, where it allows medical personnel to analyze the interior of body parts such as tissues and organs [1]. The technique has also found its use in other scientific fields such as mineralogy [2] and material sciences [3, 4].

Imaging with CT can be performed utilizing phase-contrast or absorption-contrast. While absorption-contrast is well suited for big and dense samples, phase-contrast is better suited for samples that are thin and weakly absorbing. CT imaging using phase-contrast requires a certain amount of coherence in the X-ray beam such that the propagating phase-shift through the sample can be recorded. Phase-contrast imaging is normally carried out at synchrotron facilities due to their X-ray sources having a higher coherence and a high brilliance. Absorption-contrast imaging does not require a coherent source, making it suitable for in-house CT instruments that utilize X-ray sources generating polychromatic radiation spectra.

The Department of Physics at NTNU has a cone-beam CT (CBCT) instrument of the type Nikon XT H 225 ST. A CT scan using this instrument can last from a few minutes and up to several hours, depending primarily on the number of projections and the exposure time of each projection. The image quality in a CT measurement depends on factors such as the presence of artifacts, focal spot blurring and the contrast between the sample constituents [5, 6]. Although the presence of artifacts can be reduced, they can rarely be eliminated entirely. Beam hardening, which is caused by the higher absorption of low-energetic photons in a polychromatic source spectrum by a sample, results in cupping and streak artifacts in the CT measurements. The beam hardening can be reduced through source filtration [1] or through the method of dual-energy CT [2, 7, 8]. However, some beam hardening will often prevail, limiting quantitative analysis of tomograms. Furthermore, the focal spot size of the X-ray source, which depends on the source power, causes a blurring in the projections that reduces the physical resolution in the reconstructed tomograms. The image quality

is reduced by these effects and that makes quantitative results using polychromatic sources difficult. A compact light source has been reported to generate in-house monochromatic X-rays [9], leading to possible in-house quantitative CT measurements in the future. Until then, optimizing CT parameters such as the tube voltage, current and exposure time is essential for obtaining good quality images.

In this thesis a computer program for simulating two-dimensional CT measurements has been developed. Although there exist several types of CT simulation software that vary in complexity [10, 11, 12], this particular software has been optimized to replicate a Nikon XT H 225 ST CT instrument that is routinely used at the department of physics at NTNU. Through CT simulations it is possible to determine the CT parameters that, for a given sample, would provide the optimal image quality using the real CT instrument. Furthermore, CT simulations of samples can provide information about which materials can be resolved in the reconstructed tomograms. This is crucial in samples consisting of objects that exhibit low absorption contrast such as intermetallics.

In the first part of the thesis the CT simulations have been optimized to faithfully model the aforementioned Nikon CT instrument. In this work, models of the polychromatic X-ray source, X-ray detector and focal spot size have been implemented and optimized to replicate the CT instrument. Moreover, the simulations have been validated with experimental data using three homogeneous and cylindrical samples and the impact of energy filters on the source spectrum has been discussed. Lastly, a sample consisting of a Ni layer and Ni_3Sn_2 phase layer sandwiched between two Si wafers has been simulated to investigate the effect that the focal spot blurring has on the physical resolution in a reconstructed tomogram.

The second part of this thesis consists of CT measurements of two samples that have been processed through Solid-Liquid Interdiffusion (SLID) [13, 14] and measured with X-ray CT [1]. The first sample, the Au-Sn SLID sample, consists of a lead zirconate titanate (PZT) substrate and a tungsten carbide (WC) material bonded together by various Au-Sn phases. The sample was measured on the Nikon CT instrument. The second sample, consisting of two wafers of Si bonded together by Ni-Sn phases, was measured at the European Synchrotron Radiation Facility (ESRF) in Grenoble, France, and further compared to monochromatic simulations for analysis.

[1] The samples were provided by Knut. E. Aasmundtveit, Andreas Larsson and Hoang Vu Nguyen at the University of Southeast Norway (USN).

Chapter 2

Theory of Computed Tomography

This section reviews some of the basic principles of the interaction between X-rays and matter and the theory behind X-ray CT through the Beer-Lambert law. Moreover, models for a polychromatic X-ray source, an X-ray detector and the focal spot size are presented. Further on, the theory of *Paganin* et. al. for retrieving phase or thickness information from phase-contrast images is presented and discussed [15]. Lastly, a review of image corrections in CT measurements and some common artifacts encountered in tomograms will be presented.

2.1 Interaction between X-rays and matter

The interactions between X-rays and matter include the photoelectric effect, Compton scattering, Rayleigh scattering, pair-production and photonuclear interactions. The two latter interactions must be accounted for when the photon energies exceed 1.022 MeV for the pair-production and several MeV for the photonuclear interactions [16]. However, in regular in-house CT instruments, the photon energies rarely exceed 1 MeV and the two effects can therefore be neglected. The three remaining interactions can be summarized into one component, the attenuation coefficient μ, as

$$\mu = \mu_{PE} + \mu_{CS} + \mu_R, \tag{2.1}$$

where μ_{PE} is the photoelectric effect, μ_{CS} is Compton scattering and μ_R is Rayleigh scattering. Figure 2.1 depicts the total attenuation coefficient and the contributions from the photoelectric effect, Compton scattering and Rayleigh scattering in the energy range 1 keV to 1 MeV for Ni. The contribution from the Rayleigh scattering is small compared to the combined contributions of Compton Scattering and the photoelectric effect at all energies [16]. For that reason, Rayleigh scattering can be neglected, leaving only the photoelectric effect and Compton scattering,

$$\mu = \mu_{PE} + \mu_{CS}. \tag{2.2}$$

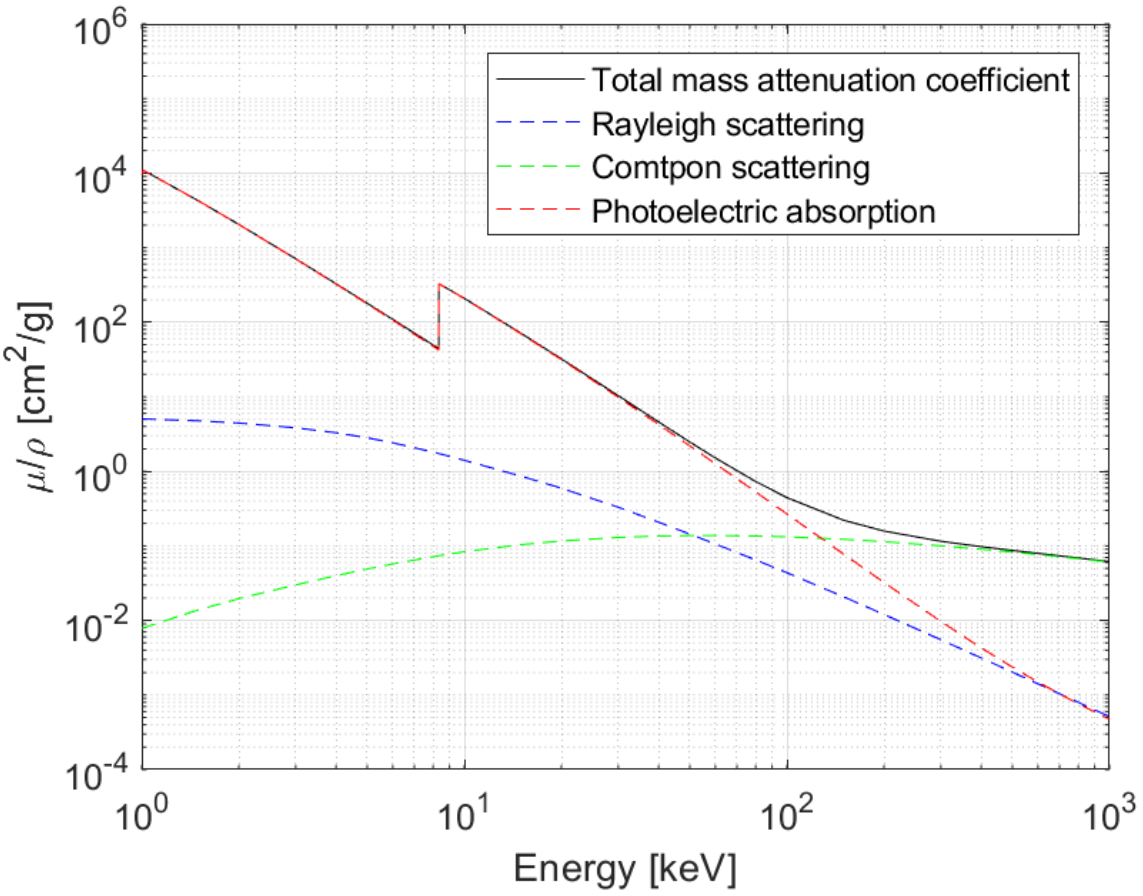

Figure 2.1: Contributions from the photoelectric effect, Compton scattering and Rayleigh scattering to the total mass attenuation coefficient of Ni in the energy range 1 keV to 1 MeV. The photoelectric effect dominates for energies below approximately 150 keV, decreasing as E^{-3}, and the Compton scattering dominates for energies above that energy. The mass attenuation coefficients have been obtained from the NIST database [17].

2.1.1 Photoelectric effect

The photoelectric effect is the absorption of an incident photon by an atom, releasing an electron from the atomic orbital and providing the electron with kinetic energy. The hole that is created when the electron is released will eventually be filled by an outer orbital electron, creating a photon with energy equal to the energy difference in the orbital transition. This process is illustrated in Figure 2.2. For the photoelectric effect to take place the binding energy of the electron must be lower than the incoming photon energy. The rest energy provides kinetic energy to the electron according to the equation

$$E_k = h\nu - E_b, \tag{2.3}$$

where E_k is the kinetic energy of the released electron, E_b is the binding energy of the atomic electron, h is the Planck constant and ν is the frequency of the incident photon [16]. The interaction cross-section of the photoelectric effect is given by

$$\mu_{PE} = K_1 \frac{Z}{A} \frac{\rho Z^{n-1}}{E^m} \tag{2.4}$$

where K_1 is a constant, Z is the atomic number, A is the atomic weight, ρ is the mass density and E is the radiation energy [16]. The exponent n in the atomic number lies in the range [4, 4.6], while the exponent m in the energy E lies in the range [1, 3], both depending on the photon energy [16]. Classically, the exponent m is equal to 3 [2]. The photoelectric effect is highly Z-dependent and will be dominant for higher atomic numbers for a given photon energy.

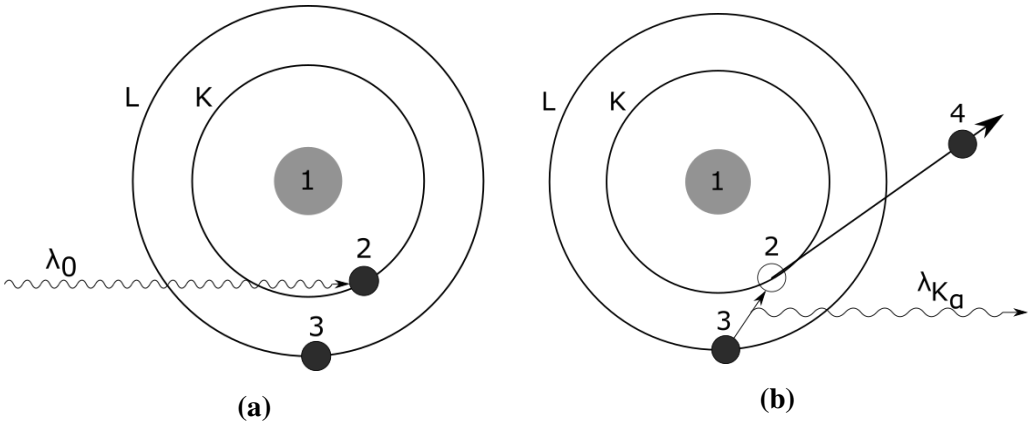

Figure 2.2: Illustration of the photoelectric effect. (a) The incident photon with wavelength λ_0 interacts with the electron. 1, nucleus; 2, electron in the K-orbital. (b) After absorption of the incident photon, the electron will be released from the K-orbital creating a hole in the atom. The hole will eventually be filled by an outer shell electron, creating a characteristic photon in the process. Here this is illustrated as a transition from the L-orbital to the K-orbital, creating a photon with characteristic wavelength λ_{K_α}. 1, nucleus; 2, hole in the K-orbital; 3, electron in the L-orbital making the transition to the K-orbital; 4, photoelectron.

2.1.2 Compton scattering

Compton scattering occurs when a photon interacts with an unbounded electron at rest. In this interaction, energy is transferred from the X-ray photon to the unbound electron and both the X-ray photon and the electron are scattered [16]. An illustration is given in Figure 2.3. Since the total mass-energy and momentum of the system are conserved during the interaction, the photon

is scattered inelastically. Furthermore, the energy of the scattered photon depends on the energy of the incident photon and the scattering angle ϕ through the equation

$$h\nu' = \frac{h\nu}{1 + \frac{h\nu}{m_c^2}(1 - \cos(\phi)}, \tag{2.5}$$

where $h\nu$ and $h\nu'$ is the photon energy before and after the collision, and m_0c^2 is the rest energy of the electron [16]. The attenuation coefficient due to the Compton scattering is given by

$$\mu_{CS} = K_2 \frac{Z}{A} \rho f_{KN}(E), \tag{2.6}$$

where K_2 is a constant and $f_{KN}(E)$ is the Klein-Nishina cross-section given by

$$f_{KN}(E) = \frac{1+\alpha}{\alpha^2}\left[\frac{2(1+2\alpha)}{1+2\alpha} - \frac{1}{\alpha}\ln(1+2\alpha)\right] + \frac{1}{2\alpha}\ln(1+2\alpha) - \frac{1+3\alpha}{(1+2\alpha)^2}. \tag{2.7}$$

Here, $\alpha = E/(m_0c^2)$ with m_0c^2 as the rest energy of the electron. The Compton scattering is, in contrast to the photoelectric effect, almost independent of the atomic number as the ratio Z/A is approximately constant. This is due to the assumption that the electrons are unbounded [16]. Moreover, the Klein-Nishina equation accounts for the relativistic effects of X-rays with energies above 100 keV. For a derivation of the Klein-Nishina cross-section, see [16].

2.2 Beer-Lambert Law

The interaction between X-rays and matter will consequently attenuate X-rays that propagate through a sample. By assuming that the incident radiation is monochromatic, the photon loss rate through a differential section in a material can be related to the attenuation coefficient and the position of the photons in the material by

$$\frac{\mathrm{d}I}{\mathrm{d}l} = -\mu I. \tag{2.8}$$

Here, I is the photon intensity of a monochromatic radiation beam, μ is the attenuation coefficient and l is the position of the photons in the material [1]. By integrating equation (2.8) one obtains the Beer-Lambert law

$$I = I_0 \mathrm{e}^{-\int_{l_0}^{l} \mu(x,y,E)\mathrm{d}l}, \tag{2.9}$$

where I_0 and I is the incident and the attenuated beam intensities at positions l_0 and l, respectively. The integral in the exponential function is the path of the beam through the sample as illustrated in Figure 2.4. The attenuation coefficient depends on both the photon energy of the monochromatic source and the type of material that the radiation propagates through from l_0 to l, so that $\mu = \mu(x, y, E)$ [1].

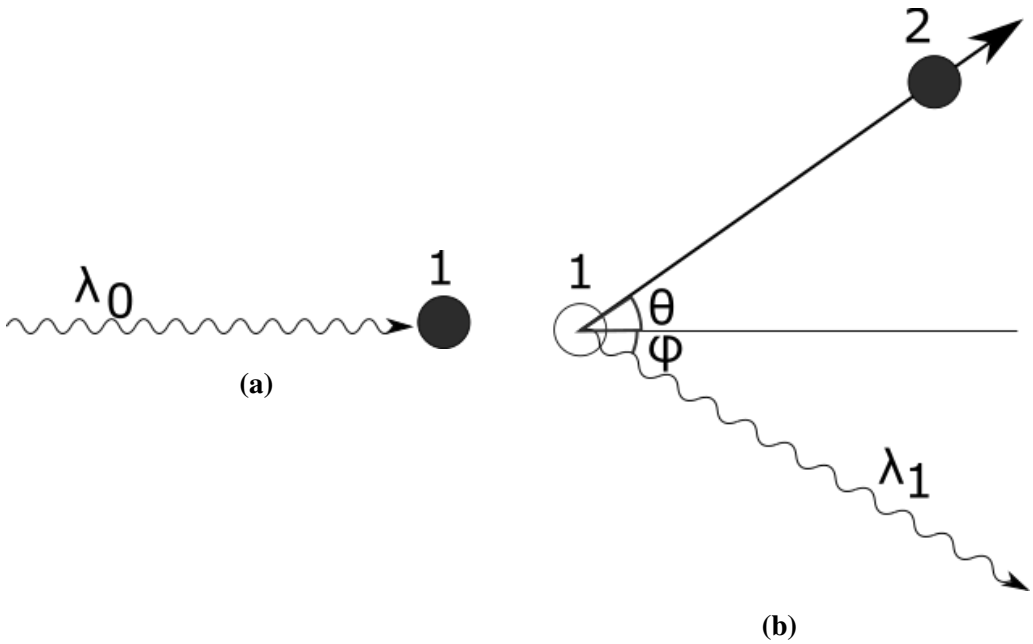

Figure 2.3: Illustration of Compton scattering. (a) The incident photon with wavelength λ_0 interacts with an unbound and stationary electron, denoted by 1. (b) The incident photon transfers a part of its energy to the electron and both the electron and the photon are scattered in the process. Due to the energy transfer, the scattered photon with wavelength λ_1 will have less energy than the initial photon energy. 1, unbound, stationary electron before the interaction; 2, scattered electron.

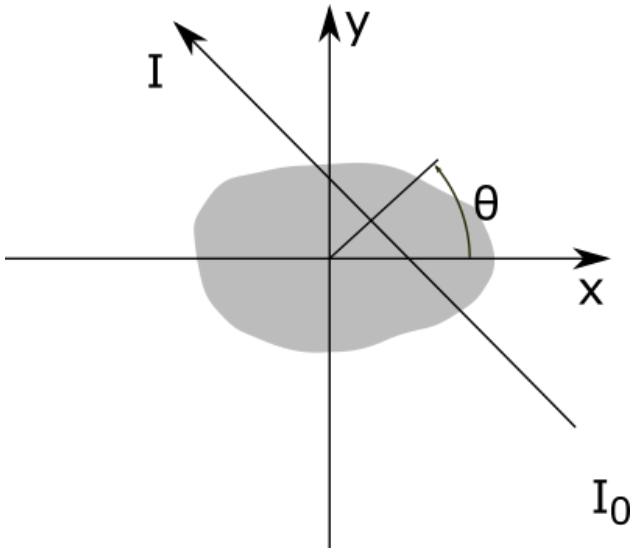

Figure 2.4: Path through the sample with I_0 as the initial photon intensity and I as the attenuated intensity. The angle θ indicates the orientation of the sample. Different projections of the sample can be obtained by rotating the sample, which changes the angle θ.

In the case where the radiation consists of a spectrum of photon energies, the Beer-Lambert law in equation (2.9) must be modified to account for both the radiation spectrum and the absorption rate of the X-ray detector. This is done by integrating over all photon energies,

$$I = \int_{E_{min}}^{E_{max}} N(V, I)S(E)D(E)\mathrm{e}^{-\int_{l_0}^{l}\mu(x,y,E)\mathrm{d}l}\mathrm{d}E. \tag{2.10}$$

Here, $N(V, I)$ is a variable introduced to account for the photon flux, depending on both tube voltage V and current I. Moreover, $S(E)$ is the normalized X-ray source spectrum modulated by the absorption materials between the source and the detector that is not part of the sample, and $D(E)$ is the detector sensitivity modulated by the protection materials on the detector. The integration limits, $[E_{min}, E_{max}]$, are the minimum and maximum energies of the radiation spectrum.

The total incident detected radiation can be determined by integrating the detected radiation over all photon energies,

$$I_0 = \int_{E_{min}}^{E_{max}} N(V, I)S(E)D(E)\mathrm{d}E. \tag{2.11}$$

By inserting equations (2.10) and (2.11) into equation (2.9) and solving the equation for the attenuation coefficient projection, one obtains [2]

$$\int_{l_0}^{l} \mu_m(x, y)\mathrm{d}l = -\ln\left[\frac{\int S(E)D(E)\mathrm{e}^{-\int_{l_0}^{l}\mu(x,y,E)\mathrm{d}l}\mathrm{d}E}{\int S(E)D(E)\mathrm{d}E}\right]. \tag{2.12}$$

This equation relates the attenuation coefficient projection to the transmitted and incident radiation I and I_0. The sample can be reconstructed from the attenuation coefficient projections using a reconstruction algorithm if a sufficient amount of projections can be obtained. The projections can be obtained by choosing different radiation paths through the sample in equation (2.12). Physically, this implies either a rotation of the sample or a rotation of both the source and the detector.

2.3 Polychromatic X-Ray Source

X-ray tube sources generate a polychromatic spectrum of photon energies and this type of X-ray sources are common for in-house laboratory CT instruments. In an X-ray tube source electrons are accelerated from the cathode towards the anode [18]. As the electrons propagate into the anode material they interact with the atomic electrons, producing an emission of continuous bremsstrahlung X-ray spectrum and characteristic X-rays. The bremsstrahlung spectrum is emitted by the electrons as they decelerate through the anode, with a maximum X-ray energy in the bremsstrahlung

spectrum equal to the voltage difference between the cathode and the anode. Superimposed on this brehmsstrahlung spectrum are the characteristic X-rays, which are caused by the phenomenon known as fluorescence. When the electron beam interacts with an atomic electron from an inner orbital in the anode, the bound electron is released and a hole is created in the atom. The hole will eventually be filled by an electron from an outer orbital in order to restore atomic stability. As the outer orbital electron has a higher energy than the inner orbital, the electron in transition will release a photon with an energy corresponding to the energy difference between the two orbitals. For instance, an electron transition from the L orbital to the K orbital is denoted a K_α characteristic X-ray, while an electron transition from the M orbital to the K orbital is known as K_β characteristic X-ray.

There exist several methods to simulate a polychromatic source spectrum. Some of the methods are based on purely empirical data [19, 20], while other methods try to model the underlying physics of the X-ray source [21]. In this thesis the X-ray source is modeled with a modified version of Kramer's law, which combines the continuous bremsstrahlung spectrum with the characteristic X-rays of the anode material [2].

$$S(E) = EK\left[\frac{1}{2\pi c}\left(\frac{E^{max}}{E} - 1\right) + K_{XRF}\sum_i k_i\delta(E - E_i)\right]\prod_i \mathrm{e}^{-\mu_i(E)z_i}. \tag{2.13}$$

Here, $S(E)$ is the source spectrum, E is the energy, K is the Kramer constant, c is the speed of light in vacuum, d is a constant, k_i is the relative intensity of characteristic peak i, and δ is the Kronecker delta. The maximum energy, E_{max}, is given by the tube voltage, known as the voltage difference between the cathode and anode. The product sum is due to the filtration material, i, between the source and the detector with attenuation coefficient μ_i and thickness z_i. As the X-rays emanate from deep within the anode material, the X-ray beam will be filtered as it propagates towards the surface of the anode material. The X-ray spectrum is further filtered by a Be window and the air between the X-ray source and the X-ray detector.

2.4 X-Ray Detector

A common way to detect X-rays is to use a Flat Panel Detector (FPD), which reads out an electronic signal using an active-matrix pixel array [22]. There are two common technical schemes for radiation detection in FPDs. The first is a direct X-ray detection scheme that utilizes photoconductors to convert the incoming X-rays into electrons [23]. The second scheme is an indirect approach as the incoming X-rays are first converted into optical photons by a scintillator material [23]. The optical photons are then detected by an array of photodiodes through absorption, which again generates electron-hole pairs that can be read by a computer through an analog-to-digital converter [24].

A scintillator works by absorption of the incoming X-rays by the bound electrons in the valence band [24]. If the energy of the incoming radiation is high enough, the electrons may be excited to the conduction band, creating an electron-hole pair that is free to move around. If, however, the amount of absorbed energy excites the electron to a state below the conduction band, then the electron will still be loosely bound. In this case, the electron and hole form a system called an exciton, which can move around in the crystal as an entity. Eventually, these excitons are trapped in an impurity or a defect in the scintillator crystal, and the excited electron dissipates its energy until it reaches the ground level in the excited state. Further on the exciton will fall down to the valence band by either emitting a scintillation photon or by releasing the excess energy thermally as phonons in the scintillator. The process of emitting a scintillation photon is called luminescence [24]. The scintillator may be thought of as a wavelength shifter, converting high energetic X-rays with a short wavelength to lower energetic optical photons with a long wavelength [25].

The efficiency of the scintillator to detect radiation can be approximated through the attenuation of the incoming X-rays [2],

$$D(E) = (1 - \mathrm{e}^{-\mu(E)l}) \prod_i \mathrm{e}^{-\mu_i(E)l_i}. \tag{2.14}$$

Here, $D(E)$ is the amount of the incoming X-rays that has been absorbed by the scintillator material in the detector, and μ and l are the attenuation coefficient and the thickness of the scintillator material. Moreover, the product sum accounts for the attenuation due to the protection layers in front of the material. The value of $D(E)$ lies between [0, 1].

2.5 Focal spot size

X-ray tube sources normally emit X-rays from a small area in a cone beam towards the X-ray detector. A simple model for such a source would be to model it as a point source. In reality, however, the X-rays are emitted from an area of finite size, increasing as the power of the source is increased in order to avoid thermal melting of the anode material. Due to this area, the measured projections will be blurred, reducing the physical resolution in the reconstructed samples. The amount of blurring depends on the magnification, meaning that projections measured with the sample placed closer to the X-ray source will be blurred more than a sample placed closer to the detector. The effect of the focal spot size is eliminated if the sample is placed at the detector.

The focal spot size of an X-ray source can be modeled as a normalized Gaussian distribution [26, 27, 28],

$$k(s) = \frac{\exp\left\{-4\left(\frac{s}{\sigma(P)}M\right)^2\right\}}{\int_{-\infty}^{\infty}\exp\left\{-4\left(\frac{s}{\sigma(P)}M\right)^2\right\}\mathrm{d}s} \tag{2.15}$$

where $k(s)$ is the focal spot distribution at the detector and depends on the position s in the projection. Moreover, $\sigma(P)$ is the Full Width at Half Maximum (FWHM) and depends on the power, P, and M is the magnification of the focal spot distribution from the source plane to the detector plane. The Gaussian distribution in equation (2.15) is convoluted with the projection $I(s,\theta)$ from equation (2.10),

$$q(s,\theta) = I(s,\theta) * k(s). \tag{2.16}$$

to give the focal spot blurred projection $q(s,\theta)$.

2.6 Noise

The noise in CT measurements consists primarily of quantum noise and electronic noise. The quantum noise is related to the generation of X-rays in the X-ray source, which follows a Poisson distribution [29],

$$P(X = x) = \frac{\mathrm{e}^{-xm}m^x}{x!}. \tag{2.17}$$

Here, m is the mean signal value and $x = 0, 1, ..$ is an integer, representing the measured signal value. The random variable X is the number of photons generated by the X-ray source. An important characteristic of the Poisson distribution is that the variance of the distribution is equal to the mean signal value, m, with a standard deviation, σ, equal to the square root of the mean signal, $\sigma = \sqrt{m}$. The signal-to-noise ratio (SNR) for a Poisson-distribution is equal to $\sqrt{N}$, with N as the photon count.

The detector absorbs a certain amount of the incoming X-rays according to the absorption rate and the X-ray detection follows the binomial distribution; it is either detected or it is not. However, a Poisson-distributed variable X going through a binomial process with probability p still follows a Poisson process, but with a signal strength of xp rather than x [29].

The electronic noise is related to the electronics of the X-ray detector and is considered to be additive white Gaussian noise [27],

$$\mathcal{N}(0,\sigma) = \frac{1}{2\pi\sigma}\mathrm{e}^{-\frac{x^2}{2\sigma}}. \tag{2.18}$$

Here, $N(\mu,\sigma)$ is the normal distribution with mean signal value $\mu = 0$ and standard deviation σ.

2.7 Monochromatic and Coherent X-Ray Source

In microtomography, using an incoherent source causes the measured intensity to be directly related to the attenuation through the sample. However, in the case of a monochromatic and coherent source, an additional effect named phase contrast is introduced into the intensity images due to the phase-propagation between the sample and the detector. In the near-field Fresnel regime, this phase-propagation causes the edges of the constituents of the sample to be enhanced in the intensity images [15]. This additional effect may be used to retrieve the phase-information or thickness-information about the sample [15]. One way to do so is through the Paganin approximation as explained by *Paganin* et al [15]. The starting point for the derivation is the transport-of-intensity equation which describes the propagation of intensity for a plane wave, given by

$$\nabla_\perp \cdot (I(\vec{r_\perp}, z)\nabla_\perp \phi(\vec{r}_\perp, z)) = -\frac{2\pi}{\lambda}\frac{\partial}{\partial z} I(\vec{r}_\perp, z). \tag{2.19}$$

Here, $I(\vec{r_\perp}, z)$ and $\phi(\vec{r_\perp}, z)$ is respectively the intensity and phase of the beam as a function of the position in the image plane $\vec{r_\perp}$ and the propagation direction z. Here, the image plane is perpendicular to the propagation direction z. Furthermore, λ is the wavelength of the plane wave, $\nabla_\perp$ is the two-dimensional gradient operator in the plane $\vec{r_\perp}$ and $\partial/\partial z$ differentiates with respect to the propagation direction z.

The derivation of the phase is based upon four assumptions [30]. It is assumed that i) the sample is homogeneous, ii) the radiation is monochromatic, iii) the incoming wave is a plane wave or a wave with low curvature, iv) the sample-to-detector distance fulfills the near-field condition, $z \ll d^2/\lambda$, where d is the smallest resolved object in the sample. If these conditions are satisfied, the projected thickness, $T(\vec{r_\perp})$, may be expressed as [15]

$$T(\vec{r_\perp}) = -\frac{1}{\mu}\ln\left(\mathcal{F}^{-1}\left\{\frac{\mathcal{F}\{I(\vec{r_\perp}, z = R_2)/I_0\}}{1 + R_2\delta|\vec{k_\perp}|^2}\right\}\right). \tag{2.20}$$

Here, μ is the attenuation coefficient of the material, R_2 is the propagation distance from the image plane to the detector plane, $\vec{k}$ is the Fourier conjugate coordinate of $\vec{r}$ and δ is the deviance from unity in the real part of the refractive index [15, 18]. The phase of the object for a sufficiently thin sample may be expressed as [15]

$$\phi(\vec{r}_\perp, z = 0) = -\frac{2\pi}{\lambda}\delta T(\vec{r}_\perp). \tag{2.21}$$

The attenuation coefficient can also be expressed through the imaginary part, β, of the refractive index [18],

$$\mu = \frac{4\pi\beta}{\lambda}. \tag{2.22}$$

By substituting the projected thickness in equation (2.20) and the attenuation coefficient in equation (2.22) into equation (2.21), and simplifying, one obtains

$$\phi(x,y) = \frac{\delta}{2\beta}\ln\left(\mathcal{F}^{-1}\left\{\frac{\mathcal{F}\{I(\vec{r_\perp}, z=R_2)}{1+(\lambda z\delta/(4\pi\beta))|\vec{k}_\perp|^2}\right\}\right). \tag{2.23}$$

The phase of the object can then be found by intensity measurements of the object in the near field Fresnel regime. After equation (2.23) has been applied to the intensity data, one may reconstruct the sample using the filtered-back projection method. The tomograms will then yield area contrast that is directly related to the material of the object [30].

The algorithm remains valid for heterogeneous samples where the ratio δ/β remains constant. This might be the case for samples with homogeneous elemental composition but with varying density [30]. In the case of a heterogeneous sample, one will observe either residual phase contrast fringes or blurred interfaces [31].

Figure 2.5a shows several latex spheres obtained with propagation-based phase contrast. Here the contrast due to absorption is low, but there is significant phase-contrast at the edges of the spheres. By using equation (2.20), the projected thickness may instead be presented as shown in Figure 2.5b.

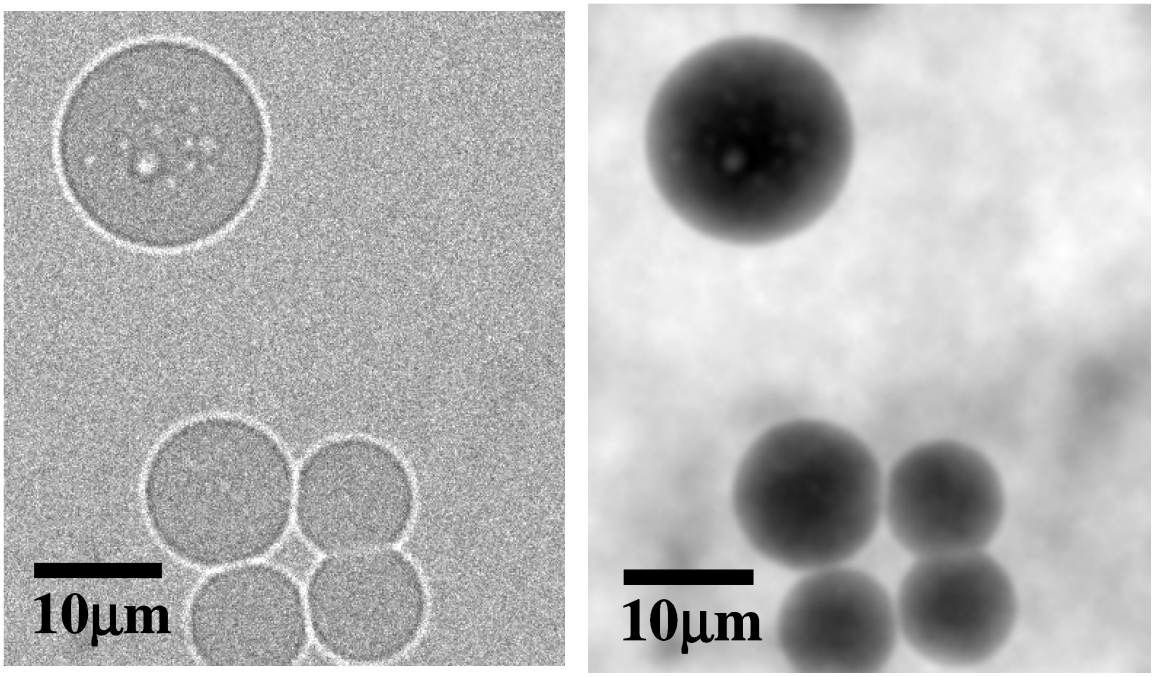

(a) **(b)**

Figure 2.5: (a) Phase-contrast image of latex spheres. (b) Projected thickness of the latex spheres obtained through equation (2.20). Images from [15].

2.8 Image Corrections in CT

Without any form of correction, the radiography images obtained by an X-ray detector will be subject to pixel-to-pixel variations. These pixel-to-pixel variations can be attributed to the non-uniform response of the X-ray detector and the non-uniformity of the emitted radiation by the X-ray source [30]. A correction for these effects can be achieved by obtaining dark field and flood field images. Dark field images are images taken with the X-ray source off, while flood field images are images taken with the X-ray source on, but without a sample. Using these images one can obtain a flat-field corrected image through the equation [30, 32, 33]

$$N = \frac{M - F}{F - D}. \tag{2.24}$$

Here, N is the flat-field corrected image, M is the measured image, F is the flood-field image and D is the dark field image. The images are two-dimensional and the subtraction and division is performed pixel-by-pixel. As there are three images included in the flat-field correction, noise will be introduced into the corrected image N. The noise can, however, be reduced by averaging several dark field and flood field images before applying equation (2.24) [32].

Bad or dead pixels may also be present in the measured pixels. However, these pixels can be removed by replacing the dead pixel value by an average of the eight neighbouring pixel values [32].

2.9 Artifacts in Polychromatic CT

There are several types of common artifacts that can appear in a reconstructed sample. These include, but are not limited to, beam hardening, ring artifacts, dark band artifacts and partial volume effects [5, 6, 34].

2.9.1 Beam hardening

The energy-dependence of the attenuation coefficients shows that the lower energy X-rays are generally more easily absorbed than the high-energy part of the radiation energy spectrum, which is due to the E^{-3} energy-dependence of the photoelectric effect [1]. Then, as the X-rays propagate through a sample it causes the average photon energy of the radiation spectrum to increase. This phenomenon is known as beam hardening and may present itself as two types of artifacts. The first is called a cupping artifact. If a cylindrical sample is measured with a CT instrument, then the X-rays passing through the center of the sample are hardened more than the X-rays passing through the edges of the cylinder. This produces a cupping artifact with higher effective attenuation coefficient values at the edges than in the center of the sample. The cupping artifact can be

alleviated by prehardening the source spectrum with an energy filter. An illustration is given in Figure 2.6.

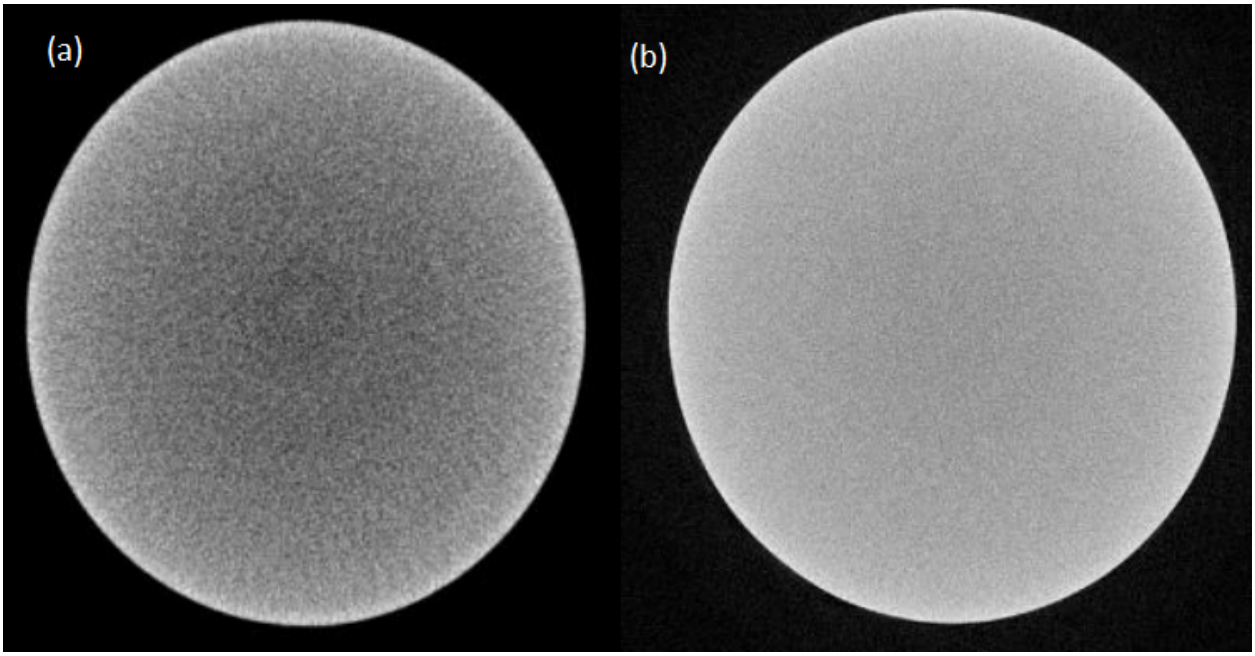

Figure 2.6: Beam hardening in the form of a cupping artifact. (a) Variations of the pixel gray values may be observed towards the center of the sample. (b) By filtering the X-ray source spectrum, the beam hardening may be alleviated. Image from Nikon Metrology.

The second beam hardening artifact is called streak or dark band artifacts. They are caused by the beam hardening that occurs between two dense objects. The X-ray spectrum will be more beam hardened when the X-rays propagate through both dense objects than when they propagate through just one of them. In the reconstructed sample this will display itself as dark bands between the dense objects [5], as illustrated in Figure 2.7.

2.9.2 Partial volume averaging

When the particles in a sample are smaller than the resolution in the reconstructed sample, the effective attenuation coefficient is a combination of the particles making up the voxel [34]. A consequence of this is that the attenuation coefficient differs from the theoretical values, which can make interpretation of such regions difficult. This effect is named the partial volume averaging effect.

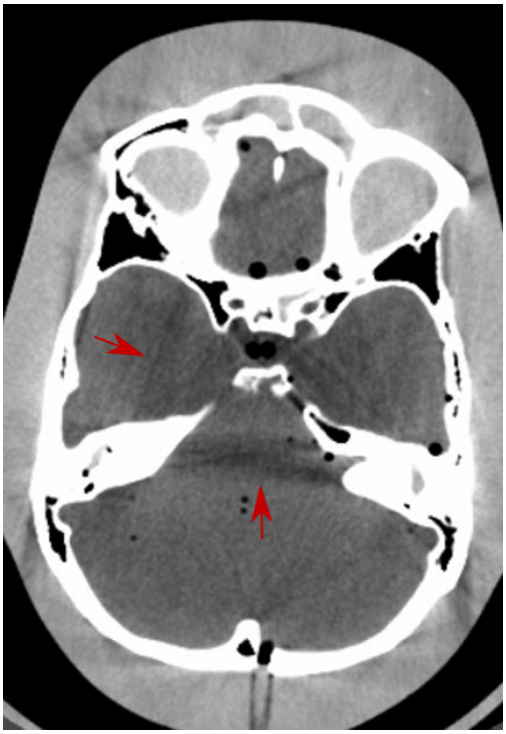

Figure 2.7: Beam hardening in the form of dark bands can be observed in the image, highlighted by two arrows. Image from [5].

2.9.3 Ring artifact

Ring artifacts in reconstructed samples occur due to the cone beam geometry of third-generation X-ray CT instruments [6, 34]. The artifact is caused by defective or miscalibrated pixels in the detector, which will give an erroneous output value of the pixel detector at all angles during the scan. When the filtered-back projection is used to reconstruct the sample, this erroneous detector pixel value will present itself as concentric rings around the axis of rotation [5]. The ring artifacts can be attenuated or completely removed by software [5], however, this increases the CT measurement time significantly.

2.9.4 Photon starvation

For high density or high atomic number samples, one may observe dark bands in the reconstructed sample. This is due to the photon starvation at the detector as the highly absorbing materials attenuate all the incoming X-rays and the detector will only measure noise [5, 34]. It is also known as the extinction artifact [6]. An illustration is given in Figure 2.8.

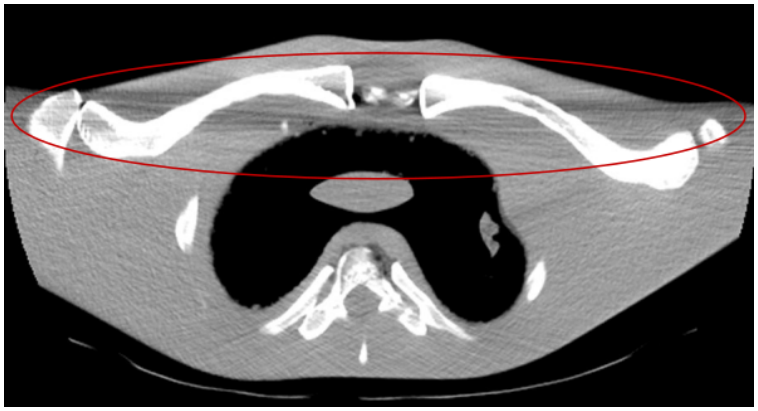

Figure 2.8: Effect of photon starvation. The white materials in the image are bones, while the encircled dark, horizontal lines shown in the image are caused by photon starvation due to the high absorption by the bones. Image from [5].

2.9.5 Anode heel effect

X-rays are generated from deep within the anode material [35]. The X-rays will therefore be filtered as they propagate through the anode material and towards the detector, and the amount of filtration depends on the angle that the anode material is oriented with respect to the incoming electron beam [36]. This causes the source spectrum to vary depending on the amount of filtration done by the anode material. This is illustrated in Figure 2.9. Although this is not classified as a traditional artifact, it is still presented under CT artifacts.

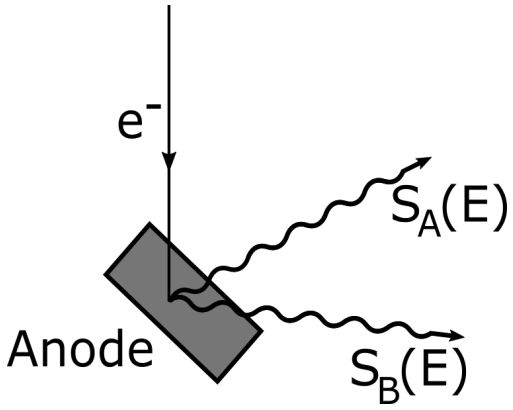

Figure 2.9: Anode heel effect. The $S_A(E)$ spectrum consists of more lower-energetic photons than the $S_B(E)$ spectrum due to the additional anode filtration of the latter spectrum.

Chapter 3

Method

In this section the various methods used in this thesis are presented. First, the working principles of the Nikon CT instrument are presented. Then the models used to generate the X-ray source and the X-ray detector are presented and the methods used to validate the simulations with measured samples are explained. Moreover, the details concerning the simulations of the cylindrical and homogeneous samples and the layered Ni-Sn sample, as well as the details of the measured AuSn SLID sample and the Ni-Sn SLID sample, are presented.

3.1 Nikon CT instrument

The Nikon XT H 225 ST CT instrument consists of a movable sample stage between an X-ray source and an X-ray detector. A photograph of the instrument is given in Figure 3.1a and an illustration of the experimental setup is presented in Figure 3.1b. In the setup, the X-rays propagate from the X-ray source towards the X-ray detector. As the X-rays propagate through the sample, the radiation is attenuated due to interaction between the matter and the radiation. The detector records a projection of the sample, and by rotating the sample one can obtain several projections at different orientations of the sample. The projections are used to reconstruct a scanned sample using the proprietary *3D Pro* software provided by Nikon. *3D Pro* uses an unknown filtered back-projection algorithm for the reconstruction.

In order to optimize the image quality one can change several settings on the CT instrument. Parameters that can be optimized before the CT scan includes the tube voltage, current, exposure time, gain, magnification and energy spectrum filter, while the voxel size, back-projection filter, reconstruction algorithm and correction algorithms can be applied after the CT scan has been performed [37]. Types of correction algorithms include scattering correction, ring artifact correction and beam hardening correction. None of the correction algorithms have been utilized throughout this thesis.

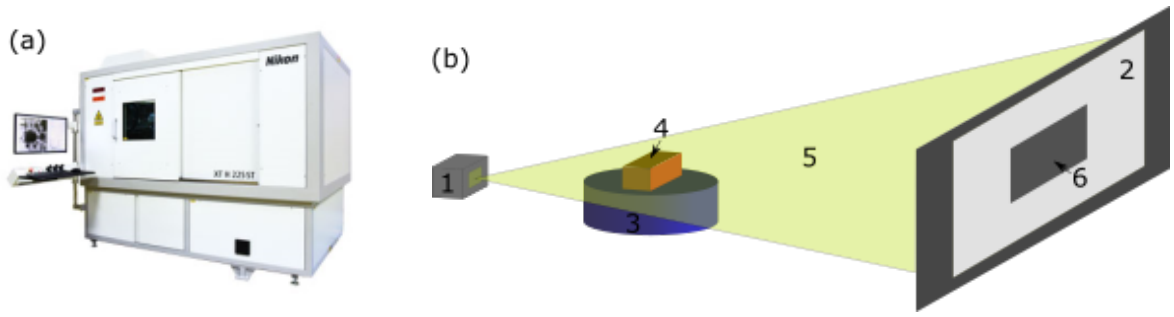

Figure 3.1: (a) Photo of the Nikon XT H 225 ST CT instrument. (b) Experimental set-up of the CT instrument; 1, X-ray source producing a polychromatic source spectrum; 2, X-ray detector converting the incoming X-rays into an electrical signal; 3, movable sample stage; 4, sample; 5, radiation propagating from the source to the detector; 6, sample projection as recorded by the detector.

3.1.1 X-ray source

The X-ray source is Nikon's proprietary 225 kV reflection target X-ray tube source with a maximum voltage of 225 kV and a maximum power output of 225 W. Nikon states that the source has a maximum focal spot width of 3 μm up to 7 W, increasing approximately by 1 μm per watt up to 225 μm at 225 W. There are four different types of anode materials that can be used: copper (Cu), molybdenum (Mo), silver (Ag) and tungsten (W).

The simulated X-ray source is based on the aforementioned source using the tungsten anode material. It is assumed that the X-rays have to propagate through 1 μm of the anode material, W. The X-ray source spectrum is further modulated by a 500 μm thick beryllium window and the air between the X-ray source and the X-ray detector, which has a distance of approximately 1.127 m. The characteristic constants k_i and characteristic energies E_i in equation (2.13) are presented in Table 3.1. Furthermore, Kramer's constant is set to $K = 1.221$ and $K_{XRF} = 0.073$ [1].

Table 3.1: Characteristic energies and the relative constant k_i for the three main characteristics K_{α_1}, K_{α_2} and K_{β_1} for W. The characteristic energies can be found from the *X-Ray Data Booklet*[38].

Variable	K_{α_1}	K_{α_2}	K_{β_1}
E_i	59.318	57.981	67.244
k_i	0.488	0.380	0.339

[1] The constants were determined using a program written by Mahsa Paziresh at Nikon Metrology.

3.1.2 X-ray detector

The X-ray detector is a Perkin Elmer XRD 1620 AN CS FPD that utilizes a scintillator material to absorb the incoming X-rays. The scintillator has a thickness of 550 μm and consists of cesium iodide (CsI) doped with thallium. The density of CsI is 4.51 g/cm^3. The detector has 2000x2000 pixels and a pitch of 200 μm with a total size of 40x40 cm^2. The exposure times of the detector can be set to 267 ms, 354 ms, 500 ms, 708 ms, 1000 ms, 1420 ms, 2000 ms, 2830 ms or 4000 ms, while the gain settings can be set to one of the values 0, 6, 12, 18 or 24. Increasing the gain by one level doubles the signal strength. Moreover, the detector has a 16 bit resolution with values ranging from 0 to 65535. The dynamical range of the detector is greater than 84 dB and the detector is operational in the energy range 40 keV to 15 MeV.

3.2 Optimization of polychromatic CT simulations

The aim of the simulation tool is to replicate the Nikon CT instrument. In order to do so, three parameters have been computed. These include an adjustable parameter $\eta(V)$ that is multiplied with the attenuation coefficients of the simulated sample, the measured or detected photon flux $N(V, I)$ and the focal spot size $\sigma(P)$. The parameter $\eta(V)$ was introduced in order to ensure approximately equal transmissions in the simulated projections and in the measured projections for a given sample, while the detected photon flux was acquired so that Poisson noise could be applied to the simulated projections. Lastly, the focal spot size was determined as it has an important effect on the physical resolution in reconstructed tomograms.

The parameter $\eta(v)$ and the detected photon flux $N(V, I)$ were determined by using a sample consisting of a layered structure. The sample consisted of a 150x150x2.5 mm^3 Al layer, a 80x150x2.5 mm^3 Al layer and a 100x100x1 mm^3 Cu layer. The positioning of these layers with respect to each other is presented in the radiography image in Figure 3.2a showing the transmission through each layer of the sample. Figure 3.2b shows two profile plots of the sample, denoting each layer.

The measurements were performed for tube voltages ranging from 100 to 190 kV with 30 kV intervals, and for each tube voltage the currents ranged from 40 to 80 μA with intervals of 10 μA, giving a total of 20 configurations. For each configuration, a flat-field correction was performed before 11 projection images were acquired of the sample. The exposure time was set to 708 ms and the gain was set to 18 throughout the measurements. The exposure time and gain were chosen such that the sample was properly illuminated by radiation for the lowest voltage and current while avoiding detector saturation for the highest voltage and current.

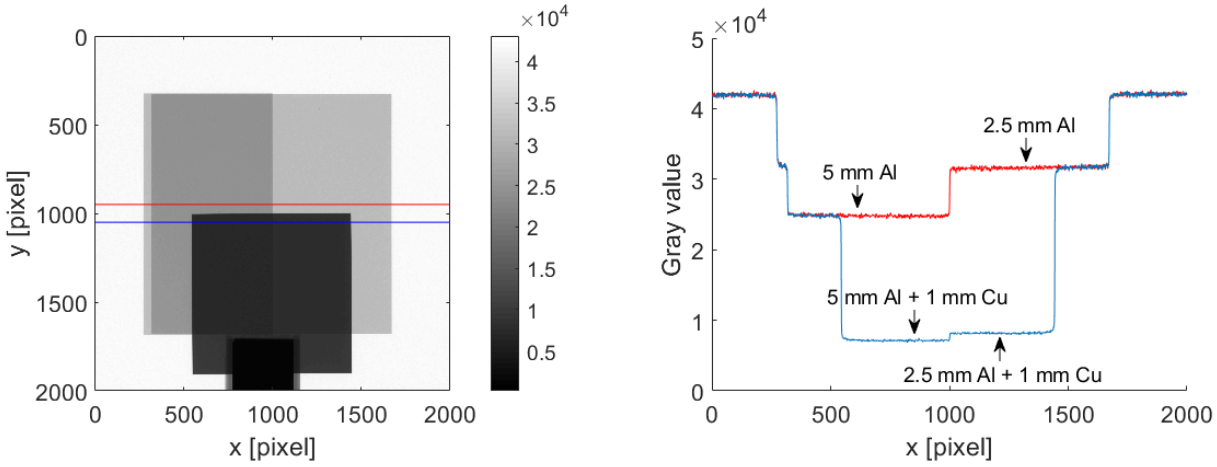

(a) **(b)**

Figure 3.2: Radiography and profile plots of the layered structure sample after flat-field correction. (a) Radiography image of the layered sample represented using gray values. (b) Profile plots from the radiography image denoting the gray values for the sample layers.

3.2.1 Estimating the parameter η

The parameter $\eta(V)$ was introduced to obtain equal transmission efficiencies in the simulated projections and in the measured projections. This was done by modifying equation (2.10),

$$I_{sim} = \int_{E_{min}}^{E_{max}} N(V,I)S(E)D(E)\mathrm{e}^{-\eta(V)\int_{l_0}^{l}\mu(x,y,E)\mathrm{d}l}\mathrm{d}E, \tag{3.1}$$

which is the equation used to obtain projections in the simulations. The parameter $\eta(V)$ was determined using an error minimization technique. To do so, the projection of the measured sample was simulated using equation (3.1). Both the measured and the simulated projections were normalized such that the projections represented the transmission through the sample with a transmission value of 1 for air. This amounts to dividing the projection with the mean value of air.

In order to reduce the presence of noise in the measured projections, the 11 recorded images of each configuration were averaged. The noise was further reduced by averaging a section of the sample for y pixel values between 1050 and 1100, resulting in an average profile plot as a function of x. The parameter was then determined by minimizing the error E in the equation

$$E = \frac{1}{N}\sqrt{\sum_{i=1}^{N}(\mu_i^m - \mu_i^s)^2} \tag{3.2}$$

where μ_i^m and μ_i^s are the mean values of the measured and simulated layer i in the sample. The Matlab optimization routine *fminsearch* was then applied to minimize the error E by varying the

parameter $\eta(V)$ in equation (3.1) and the initial guess for $\eta(V)$ was set to 1. The procedure was repeated for each configuration of the tube voltage and current.

3.2.2 Estimating the photon flux

An estimate of the measured photon flux $N(V, I)$ has to be obtained in order to apply Poisson noise to the simulated projections. In this thesis, estimates were obtained by comparing the applied Poisson noise in the simulated projections with the noise in the measured projection images for the layered sample.

The layered sample was simulated and a projection was obtained using equation (2.10) with an initial guess of the photon flux $N(V, I)$ equal to $3 \cdot 10^8$. Poisson noise was then applied to the projections using a Poisson random number generator function *imnoise*. The photon flux was then optimized by minimizing the error E in the equation

$$E = \frac{1}{N}\sqrt{\sum_{i=1}^{N}(\sigma_i^m - \sigma_i^s)^2}. \tag{3.3}$$

Here, σ_i^m and σ_i^s is the measured and simulated standard deviation, respectively, of each layered structure i in the sample. E is the square root of the sum of the differences in standard deviations in each layer. The total error E was minimized by varying the constant N in equation 2.10 using the optimization routine *fminsearch*. The procedure was repeated for each configuration of the tube voltage and the current.

3.2.3 Measuring the focal spot size

The focal spot size was estimated by determining the standard deviation σ in the Gaussian focal spot distribution in equation (2.15). A 2 mm in diameter cylindrical and homogeneous carbon steel sample with a density of 7.86 g/cm^3 was used. The sample was highly magnified by placing the sample close to the X-ray source. A high magnification is required such that the penumbra, which is the focal spot blurring area, can be observed. The setup for the cylindrical sample placed vertically on the sample stage is presented in Figure 3.3. In the figure, d is the apparent focal spot size, L_{SO} and L'_{SO} is the source-object distance and the source-projected object distance, L_{SD} is the source-detector distance and r is the radius of the object. Furthermore, P is the penumbra and U is the umbra [36]. The CT instrument indicated a magnification of 101.5, however, a discrepancy of this value is expected due to tilting of the sample, the distance L'_{so} is not equal to L_{so}, and L_{so} is not equal to the center of rotation of the sample stage.

The cylindrical sample was measured for a constant tube voltage of 100 kV, an exposure time of 708 ms with the gain set to 18. The currents ranged from 10 to 30 μA in 1 μA intervals. The ex-

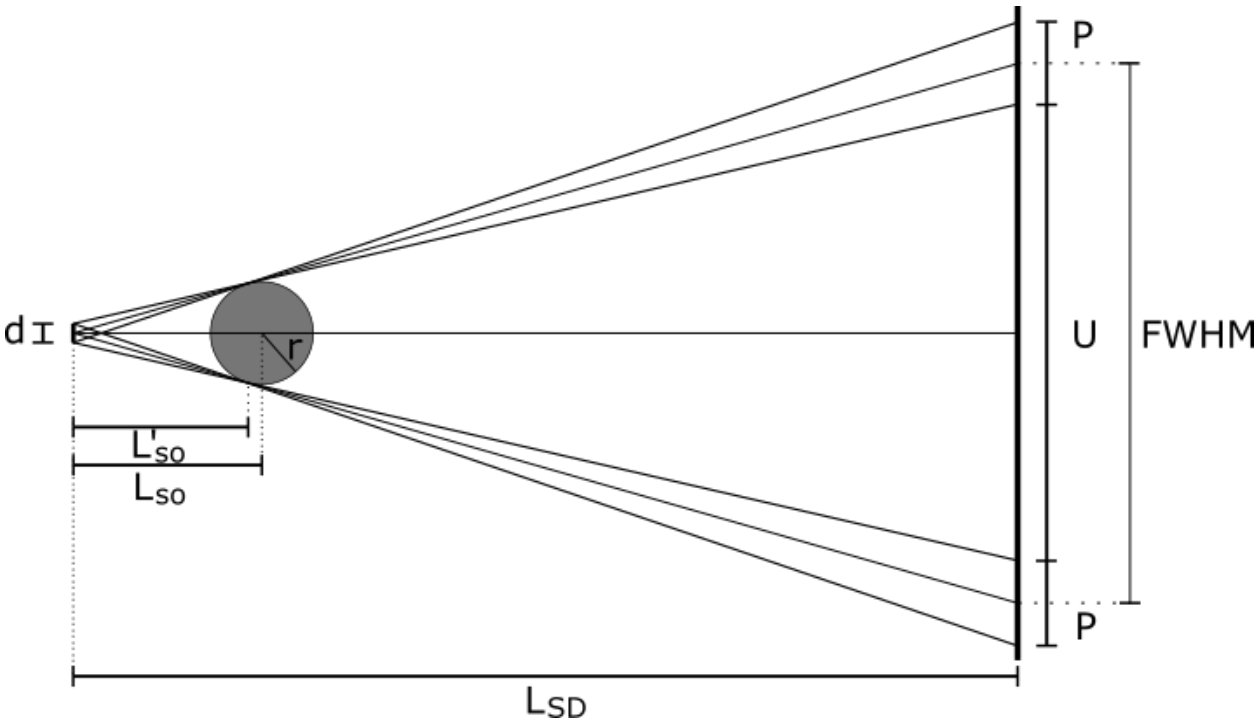

Figure 3.3: Effect of the finite size of the X-ray source for a cylindrical sample with radius r, source-object distance L_{so} and source-detector distance L_{sd}. The sample was orientated vertically on the sample stage.

posure time and gain was set so that saturation of the detector was avoided at 30 μA. Before each measurement the CT system was flat-field corrected and an average of 64 images were acquired for each configuration to reduce the noise. The noise was further reduced by averaging a section in the y-direction of the sample, giving one line profile as a function of x. The averaged section is illustrated in Figure 3.4 as the section between the two red lines.

As the X-ray source has a cone-beam geometry, equation (2.10), which assumes a parallel source geometry, cannot be used to simulate the projected sample. Instead, a simple fan-beam geometrical model using a point source was implemented to simulate the projected cylindrical sample. The simulated point-source projection was convoluted with the Gaussian distribution in equation (2.15) and compared to the measured sample. The standard deviation σ in equation (2.15) and the magnification M were determined by minimizing the error E in the equation

$$E = \frac{1}{N}\sqrt{\sum_{x=1}^{N}(I_{meas}(x) - I_{sim}(x))^2}, \tag{3.4}$$

where I_{meas} and I_{sim} are the measured and simulated projections, respectively. The number of pixels N is 2000. The *fminsearch* routine was used in the minimization.

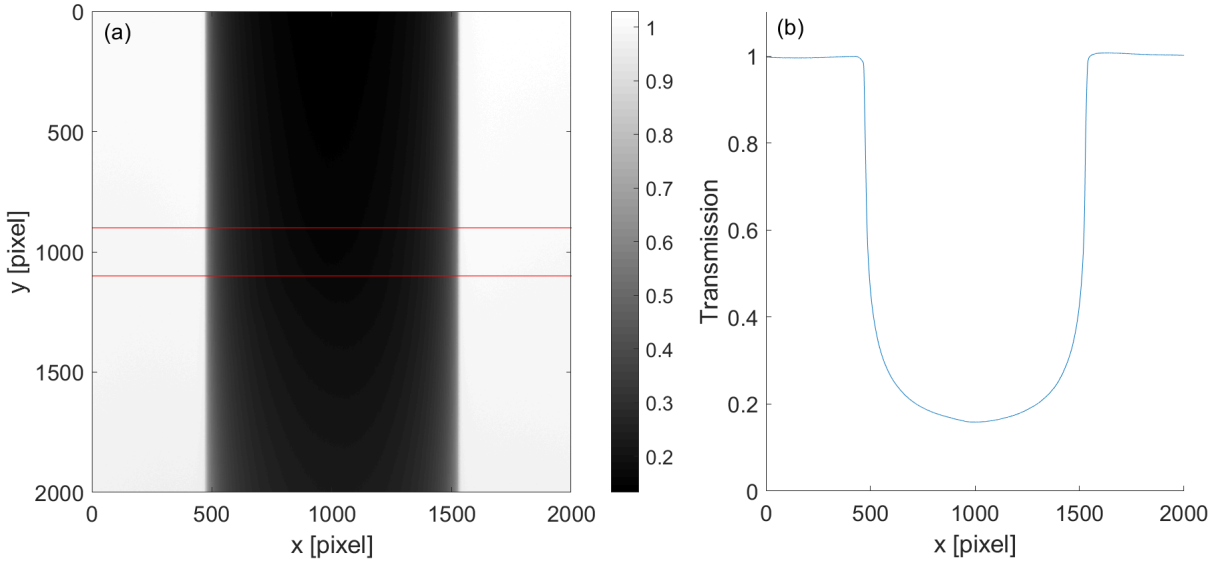

Figure 3.4: (a) Radiography image of the cylindrical sample used to determine the focal spot distribution. (b) Profile of the sample obtained by averaging between the two red lines in (a).

The obtained Gaussian distribution lies in the image plane. In order to go from the image plane to the source plane, the standard deviation must be divided by the magnification M. In this thesis, the focal spot size is defined as the Full Width Half Maximum (FWHM), σ, as in equation (2.15).

3.3 Polychromatic CT simulations and measurements

Here, the samples that have been measured and simulated using polychromatic CT in the thesis are presented, starting with the cylindrical and homogeneous samples and continuing with the simulation details of the layered Ni-Sn sample. Lastly, the measurement details of the Au-Sn SLID sample is presented.

3.3.1 Cylindrical and homogeneous Samples

The simulations were validated with real measurements with a simple test case using three cylindrical samples. Additionally, cylindrical samples have rotational symmetry, making the cupping artifact easily detectable in the reconstructed tomograms. The effect of filters on the cupping artifact is therefore also easily studied using cylindrical samples.

The three cylindrical samples consist of polyoxymethylene (POM), polytetrafluoroethylene (Teflon) and Al, and their composition, density and cylinder diameter are presented in Table 3.2. The sam-

ples were chosen due to the difference in absorption of radiation. It is expected that a material such as Al will attenuate the incoming X-rays more efficiently than the two polymers, POM and Teflon.

The CT settings were set to 135 μA, 1571 projections, gain equal to 12 and the magnification provided a pixel size of 24.03 μm. The three samples were measured at 120 kV and the Al sample was also measured using a 0.25 mm Cu filter. The CT instrument was flat-field corrected before each CT measurement and the proprietary *3Dpro* software was used to reconstruct the samples. The reconstruction algorithm used an unknown implementation of the ramp filter.

Like the CT measured samples, the simulations were computed with a tube voltage of 120 kV and a current of 135 μA. The pixel size was set to 24.03 μm and 1571 projections were obtained. A Ram-Lak filter was used in the filtered-back projection reconstruction algorithm. The reconstructed tomograms for both the simulations and the CT measurements were scaled to values between 0 and 1. This was done by subtracting the average air value from the tomograms and then dividing by an average maximum value of the tomograms.

Table 3.2: Composition, density and diameter of the three homogeneous and cylindrical samples used to validate the simulations with real CT measurements.

Sample	Composition	ρ [g/cm^3]	Diameter [mm]
Aluminum	Al	2.70	6.0
POM	CH_2O	1.42	8.4
Teflon	C_2F_4	2.20	10.2

3.3.2 Layered Ni-Sn samples

A Ni-Sn layered sample is studied here due to the interest of Ni-Sn systems processed with Solid-Liquid Interdiffusion [13, 39]. Such processed samples are of particular interest in microelectronics used in extreme environments as the Ni-Sn phases created during the interdiffusion process have a higher melting point than the lowest melting point material, Sn [13].

Samples consisting of thin layers or small regions of Ni-Sn phases are difficult to distinguish using a polychromatic CT instrument based on absorption-contrast. This is due to the similar attenuation coefficients of the Ni-Sn phases. As the layers are thin, they may be blurred out by both the reconstruction algorithm and the focal spot size. In addition to this, beam hardening makes phase discrimination even more difficult.

Here we simulate a layered sample consisting of Si/Ni/Ni_3Sn_2/Ni/Si to determine how thick the Ni_3Sn_2 must be in order to resolve it on the real CT instrument. The beam hardening effect is also

studied. In these simulations the focal spot size is important as it has a significant impact on the physical resolution. Three simulations were performed with the setting presented in Table 3.3. The pixel size was set to 4 μm and the layer thicknesses of Ni was 48 μm and the total sample size was 1.5x1.5 mm^2. A Ram-Lak filter was used in the reconstruction algorithm.

Table 3.3: Measurement settings for the polychromatic simulation of the layered Ni-Sn sample. Each phase has the same thickness and the simulations were performed with a constant tube voltage of 180 kV and 1571 projections.

Sample	Ni_3Sn_2 layer thickness [μm]	Current [μA]	Filter
Sample 1	64	100	1.0 mm Cu
Sample 2	64	100	1.0 mm Ag
Sample 3	56	10	1.0 mm Cu

3.3.3 Layered Au-Sn SLID sample

The layered Au-Sn SLID sample consists of a PZT die of 5x5x0.35 mm^3 and a Tungsten Carbide (WC) substrate of 5.5x6.5x0.21 mm^3 bonded together by various Au-Sn phases. The sample had been cut into five pieces and the centerpiece of the sample was measured using the Nikon CT instrument. The sample was measured with a tube voltage of 180 kV, current of 65 μA, 1571 projections, exposure time of 2.0 s and using a 0.125 mm Ag filter. The reconstructed tomograms had a voxel size of 3.69 μm^3.

The reconstructed tomograms were reorientated using *VGstudio* and further rendered in three dimensions using isovalues. Two dimensional cross sections are also presented.

3.4 Synchrotron measurement of a Ni-Sn SLID sample

A Ni-Sn SLID sample was measured at the European Synchrotron Radiation Facilities (ESRF) at the ID19 beamline in Grenoble, France, using a monochromatic and partially coherent radiation source at 105 keV. Due to the coherence of the beam, the Paganin approximation was applied to the measured intensity projections to transform the combined phase and absorption contrast into attenuation values [30], and the sample was reconstructed using the filtered-back projection. The voxel size was 2.25 μm^3.

The sample consisted of a layered structure with two Si substrates and a bonding layer, and had been processed with the Solid-Liquid Interdiffusion (SLID) technique forming different phases throughout the bond layer [13, 14, 39].

A monochromatic simulation of the Ni-Sn sample was also computed with an assumed structure of the sample presented in Table 3.4. Additionally, an air pocket and a Ni layer was placed in certain positions in the Ni_3Sn_2 layer. An illustration of the sample is presented in Figure 3.5. Both the source strength and the detector response was set to 1, and 2500 projections were used. Additionally, an appropriate amount of white Gaussian noise was added to the simulated projections such that the noise in the simulated projections was approximately the same is in the measured sample. The reconstructed sample was scaled using the average value of Si of 65 and an assumed value of 254 for Sn from the sample measured at ESRF. This was done so that a comparison could be conducted.

Table 3.4: Structure of the simulated sample. The layer thickness, density and attenuation coefficient for each material and phase in the structure are presented. The structure is Si/Ni/Ni_3Sn_2/Ni/Si. The last Si layer is 531 μm. The densities were retrieved from *Springer Materials* [40].

Material	Size [μm]	ρ [g/cm^3]
Si	549	2.33
Ni	4.5	8.90
Ni_3Sn_2	6.75	8.75

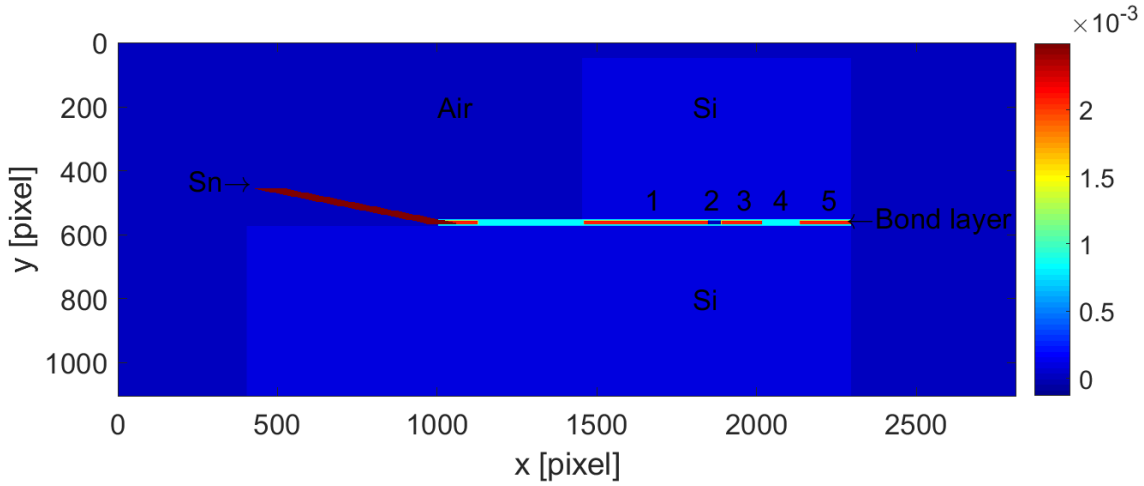

Figure 3.5: Simulated layered NiSn sample represented with attenuation coefficients before CT simulation. 1, 3 and 5 are Ni_3Sn_2 layers while 2 is an air pocket and 4 is a Ni layer.

Chapter 4

Forward Polychromatic CT Simulations

In this chapter, the simulation tool based absorption contrast is presented. The chapter starts by giving an explanation of how a sample is simulated using attenuation coefficients. It continues by going through the simulation work flow step by step. Lastly, some thoughts and comments on the simplifications used in the simulations are presented.

4.1 Simulating a sample

In the case of monochromatic radiation a sample can be represented by a two-dimensional matrix, where the elements in the matrix are filled with attenuation coefficients that correspond to the monochromatic radiation energy. For instance, if the sample consists of silicon (Si) and the radiation energy is E, then each element in the matrix will be filled with $\mu_{Si}(E)$. This implies that the distance between any two elements in the matrix is a measure of length. If the attenuation coefficient is given in μm^{-1}, then the length between two neighbouring matrix elements is equal to 1 μm. For an NxM matrix the first direction will be N μm and the second direction will be M μm, with N, M integers.

When the X-ray source generates an X-ray spectrum instead of monochromatic radiation, the energy-dependence of the attenuation coefficients must be accounted for as well. This is done by setting up a three-dimensional matrix, where the third dimension is filled with the attenuation coefficients as a function of photon energies. For instance, if the energy spectrum has a range $E \in [1, 150]$ keV with increments of 1 keV, then the third dimension will have size 150 with $\mu(E_1)$ to $\mu(E_{150})$.

The mass attenuation coefficients were retrieved from the *X-Ray Attenuation and Absorption for Materials of Dosimetric Interest* (XAAMDI) database from *National Institute of Standards and Technology* (NIST) [17]. The XAAMDI database provides mass attenuation coefficients in the

atomic number range 1 through 92 in the energy range 1 keV to 20 MeV. In addition to this, the mass attenuation coefficients for 48 compounds are listed. As the mass attenuation coefficients are spaced in an interval of 10 coefficients per energy decade, interpolation was used to obtain a higher energy resolution. The log-log plot of the attenuation coefficients in Figure 2.1 is linear up to the K edge, which is due to the E^{-3} of the photoelectric effect [2]. However, Compton scattering becomes more important for higher energies and the log-log plot starts to curve. For these reasons, the logarithm of the mass attenuation coefficients was linearly interpolated up to the K edge while a polynomial interpolation 'Piecewise-Cubic Hermitian Interpolating Polynomial' (*pchip*) was used on the remaining attenuation coefficients [41]. A spacing of 1 keV between each attenuation coefficient was used in the simulations in this thesis.

4.2 Cascaded linear-systems theory

The work flow of the simulations can be represented by a cascaded linear system [27], as illustrated in Figure 4.1. The simulations start by simulating the source spectrum and the detector sensitivity. For each energy in the range E_1 to E_N, the radon transform computes a projection, $p(s, \theta, E_i)$, for the sample. The Matlab function *radon* is used to compute the projections. The projections, $p(s, \theta, E_i)$, are then summarized by a for-loop, giving $p(s, \theta)$. Then the projections are convoluted with the focal spot distribution,

$$q(s, \theta) = p(s, \theta) * k(s), \tag{4.1}$$

where $k(s)$ is the focal spot distribution given in equation (2.15). Before the convolution can be computed the projections are padded with the signal I_0 given in equation (2.11). The Matlab routine *conv* is used to compute the convolution. The next step applies Poisson noise to the convoluted projections $q(s, \theta)$,

$$n(s, \theta) = \text{Poiss}(p(s, \theta)), \tag{4.2}$$

where $n(s, \theta)$ is the projections applied with Poisson noise and Poiss() is a function that returns a random number from the Poisson distribution based on the photon flux in $q(s, \theta)$. The Matlab routine *imnoise* is used to apply the Poisson noise. The last step calculates the projected effective attenuation coefficients $\mu_{eff}(s, \theta)$,

$$\mu_{eff}(s, \theta) = -\log\left(\frac{q(s, \theta)}{\sum_E I(E)}\right). \tag{4.3}$$

Reconstruction is then performed using the filtered-back projection routine *iradon*. The function *iradon* is the inverse Radon transform is based on the Filtered Back-Projection (FBP) algorithm. Although several types of filters may be applied, only the Ram-Lak filter is a ramp-filter that does not suppress high frequencies in the sample. This leaves the finer details in the tomograms at the

expense of more noise. The function works by applying the filter in the frequency domain by multiplication with the projections. Then the filtered projections are zero-padded to order 2 to avoid spatial-domain aliasing. Lastly, the inverse fast Fourier transform (FFT) is applied to the projections to reconstruct the simulated sample.

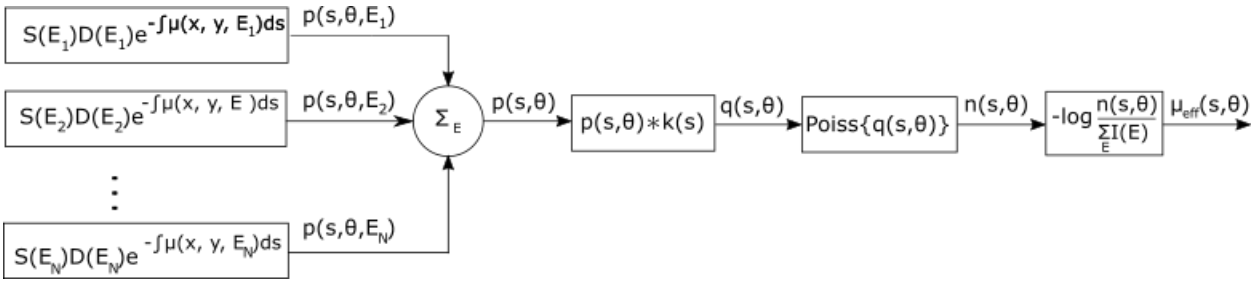

Figure 4.1: The steps in the CT simulations in the form of a cascaded linear system. The first step calculates the projections as a function of energy, giving $p(s,\theta,E_i)$. The second step summarizes the energy-dependence of the projections into one variable, $p(s,\theta)$. The third step convolutes the projections with the focal spot distribution and the fourth step applies Poisson noise. The final step calculates the projected effective attenuation coefficients.

4.3 Simplifications

The CT simulation software has been simplified in certain ways. The first simplification is that the CT simulations are limited to two dimensions. As most of the computational time is spent on computing the sample projections, restricting the simulations to two dimensions makes the simulations possible on a standard laptop.

Second, the CT simulation assumes a parallel beam geometry that differs from the cone-beam geometry of the Nikon CT instrument. Due to the divergence of the beam in the CT instrument, differences will be observed in the projections of the simulations and the real CT measurements farther from the optical axis.

Third, the interactions due to the Compton and Rayleigh scattering are included in the attenuation coefficients, however, they are treated as an absorption and none of the scattered X-rays will be detected by the X-ray detector.

Chapter 5

Results and Discussion

This chapter starts by presenting the results from optimizing the simulation software to the CT instrument, which include the parameter $\eta(V)$, detected photon flux $N(V, I)$ and the focal spot distribution $\sigma(P)$. The next part presents the simulations and CT measurements of cylindrical samples. Then the effect of the focal spot size on the physical resolution in tomograms is discussed through simulations of a layered Ni-Sn sample. The chapter continues by presenting the results for the Au-Sn SLID sample, and a discussion on the presence of artifacts in the reconstructed tomograms follows. Finally, the results for the Ni-Sn sample measured at ESRF are presented and discussed, and then compared to a sample simulated using monochromatic and incoherent radiation.

5.1 Parameter η

The parameter $\eta(V)$ must be determined before the measured photon flux can be acquired. Figure 5.1 presents plots of the estimated parameter $\eta(V)$, obtained by minimizing the difference between the measured and the simulated projections as a function of the tube voltage. Five of the plots correspond to the five different currents, while the two last plots correspond to the average value of the five plots of the currents and the line that was fit to the average parameter $\eta(V)$. The linear fit does not match the data points well, having an R^2 value of only 0.61. This gives a large discrepancy, especially for the tube voltage around 160 kV. When simulations are performed, the average parameter $\eta(V)$ has been used, and linear interpolation was used to obtain the parameter $\eta(V)$ between the measured tube voltages.

Figure 5.2 presents four comparisons of measured and simulated projections at the optimized parameter $\eta(V)$. Figures 5.2a and 5.2b are comparisons for a tube voltage of 100 kV and currents of 40 μA and 80 μA, respectively, while Figures 5.2c and 5.2d is the same comparison for a tube voltage of 190 kV and currents of 40 μA and 80 μA, respectively. In the case of a tube voltage

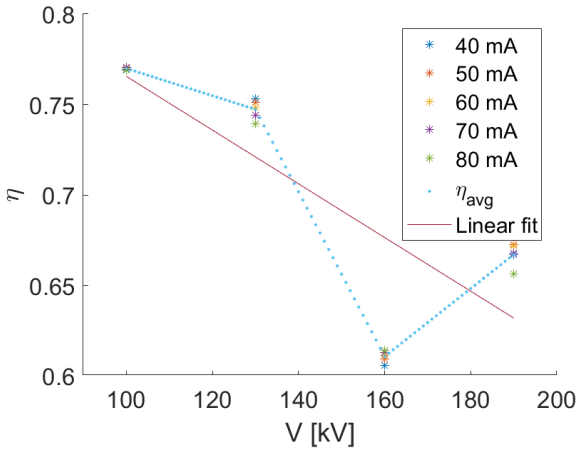

Figure 5.1: Estimated parameter $\eta(V)$ as a function of tube voltage and current. The line was fitted to the η_{avg} as a function of tube voltage with R^2=0.61.

of 100 kV, a good correlation between the measured and simulated projections can be observed. However, as the tube voltage increases to 190 kV, the discrepancy increases as well. The simulated and measured projections still fit remarkably well, as shown in the relative error plots in Figure 5.3. The sharp peaks that can be observed in the figure are due to differences in the simulated sample and the real sample. These sharp peaks do not affect the results, as the error is minimized between these peaks. It can be observed that the relative error between the peaks lies below 10 %, and that the relative error is larger for tube voltages of 190 kV.

It is important to understand why a parameter $\eta(V)$ is needed to obtain similar measured and simulated transmission projections. The physical interpretation of a parameter $\eta(V)$ lower than unity is that either the path length through the materials is overestimated or that the attenuation coefficients are underestimated. The thicknesses of the Al and Cu layers were measured with a capillary with a precision of ±0.05 mm. As the parameter is below 0.8, indicating that the material thicknesses are more than 20 % lower than the measured values, the deviation may not be explained by imprecise measurement of the sample thickness.

There are two more reasonable explanations for the need of a parameter $\eta(V)$ to match measured and simulated data. First, it is believed that there is a discrepancy between the simulated X-ray source spectrum and the real spectrum. Future work should therefore evaluate the correctness of the simulated X-ray spectrum. Second, the thickness of the protection layer in front of the detector is not known as this is proprietary information of the X-ray detector manufacturer. It was therefore set to 0 in the computations performed in this thesis. Although that is physically unreasonable, the results using no protections layer provided a better match between simulated and measured projections than with a protection layer.

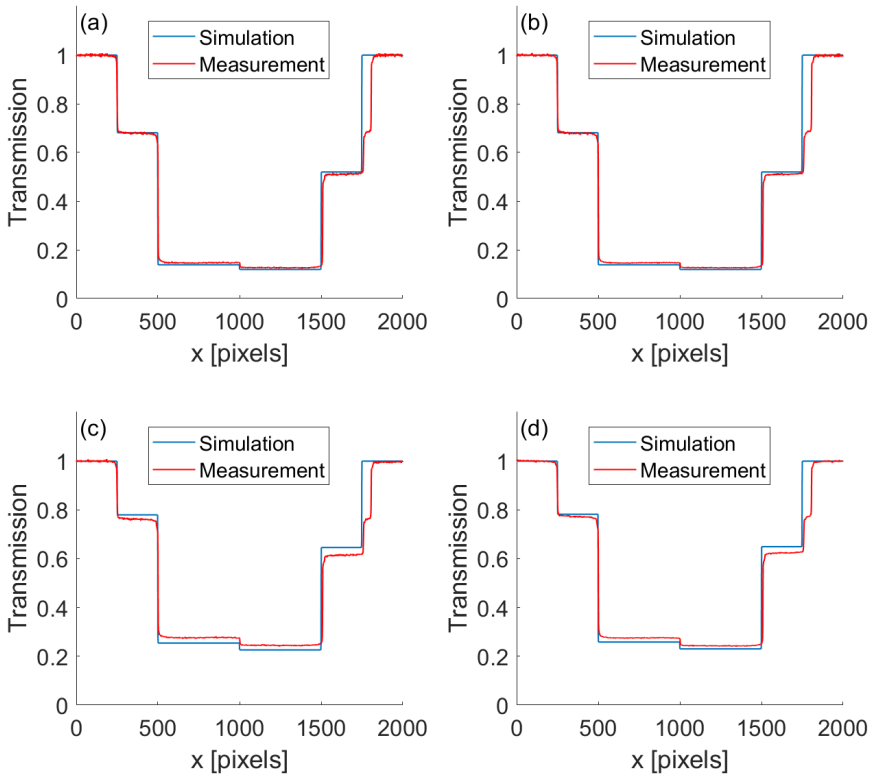

Figure 5.2: Projections of the Al and Cu layered sample at the optimized $\eta(V)$. Four different configurations of the tube voltage and the current. (a) $V = 100$ kV and $I = 40$ μA, (b) $V = 100$ and $I = 80$ μA, (c) $V = 190$ kV and $I = 40$ μA and (d) $V = 190$ kV and $I = 80$ μA. The figures show a good correlation between the measured and simulated projections. There is also a considerable amount of noise in the two center layers.

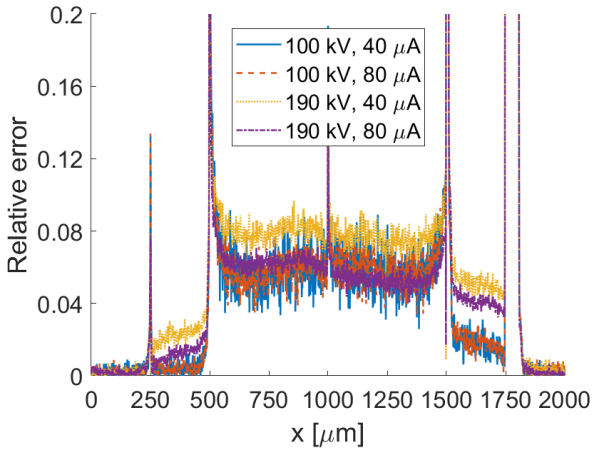

Figure 5.3: The relative error between measured and simulated projections. The sharp peaks that can be observed close to the boundaries between different layers are due to differences between the simulated sample and the real sample, and are not of interest. Note that the relative error is below 10 % for all regions between the sharp peaks.

5.2 Measured photon flux

The detected photon flux was determined in order to apply Poisson noise to the simulated projections. Figure 5.4a presents the detected photon flux adjusted for the anode current, the exposure time and the pixel size, presented as a function of the tube voltage. It is the measured photon flux obtained by propagating through air from the source to the detector and is therefore a measure of I_0. The linear fit to the average of the adjusted detected photon flux has an R^2 value of 0.94, showing a linear correlation between the detected photon flux and the tube voltage. Figure 5.4b presents similar results for the photon flux per detector pixel.

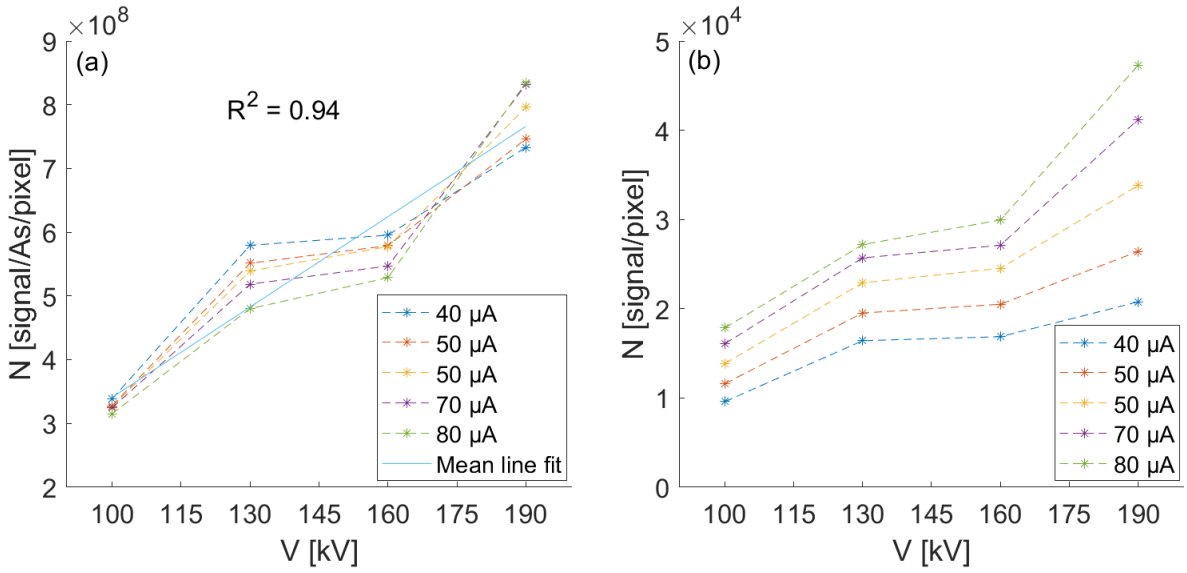

Figure 5.4: (a) Measured photon flux per ampere second detected by a pixel and (b) measured photon flux detected by a detector pixel, increasing for higher currents.

A comparison between the simulated and measured noisy projections of the layered Al and Cu sample is presented in Figure 5.5. The dependence of the transmission efficiency on the amount of noise is clearly visible in the figures, showing increased noise with higher transmissions. It should be noted that as the method used to estimate the detected photon flux depends implicitly on the transmission, it is paramount that the simulated projections have a transmission rate similar to that of the measured projections. In Figures 5.5c and 5.5d a discrepancy between the simulated and measured projections can be observed, as noted in the previous section. In the case of the Al layers the simulated projections have a higher transmission rate than the measured projections and will thus be noisier. The same argument can be used on the combined Al and Cu layers, where the simulated projections have a lower transmission rate than the measured projections, resulting in less noise in the simulated projections.

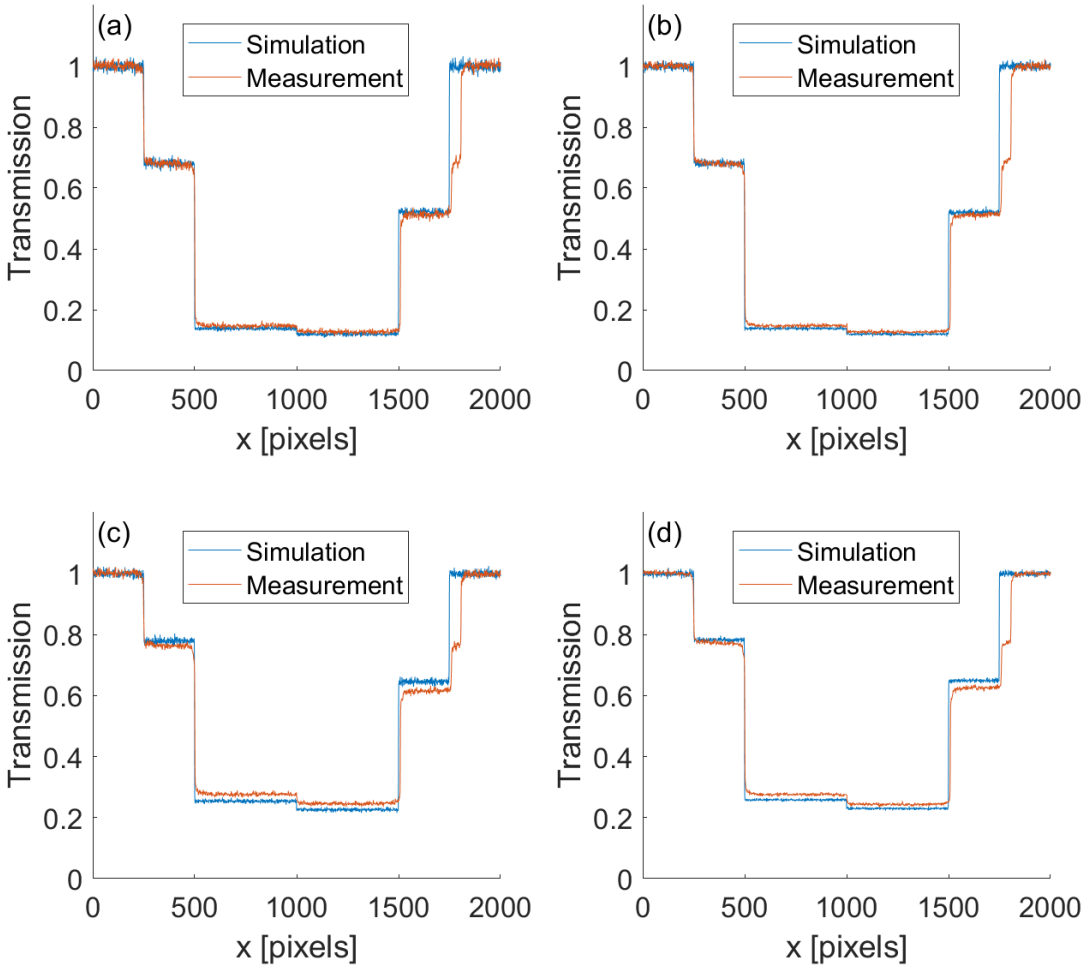

Figure 5.5: Normalized measured and simulated transmission for the layered sample with Poisson noise. The signal dependence of the noise is clearly visible, depending on the transmission. (a) V = 100 kV and I = 40 μA, (b) V = 100 and I = 80 μA, (c) V = 190 kV and I = 40 μA and (d) V = 190 kV and I = 80 μA.

5.3 Focal spot size

The measured focal spot size σ as a function of power is presented in Figure 5.6a. The linear fitted line indicates a focal spot size starting at 29.3 μm at 7 W, increasing with 0.28 μm/W. The line has an $R^2 = 0.89$. To avoid melting the anode target as the power increases, the electron focusing device in the source creates a larger focal spot size such that the heat can be dissipated over a larger area. It is therefore expected that the focal spot increases with increased power.

Nikon guarantees that the focal spot size is 3 μm up to 7 W and increases with approximately 1 μm per watt, which is different from the results presented here. Nikon uses finely engineered masks consisting of strips of a high absorptive material to determine the size of the focal spot. These are produced by Japan Inspection Instruments Manufacturers Association (JIMA) and has been used by Hiller et. al. to confirm their results [42].

There are several ways to test the validity of or improve the results presented here. First, the cylindrical sample used in these measurements may be replaced by a smoother and more perfectly cylindrical sample. This might improve the fit between measured and simulated projections overall. Second, other focal spot distributions may be investigated such as the sigmoid functions that are variations of the Fermi-Dirac distribution [36].

The optimized magnification as a function of power is presented in Figure 5.6b. The sample was placed close to the source to obtain the highest possible magnification. This was done so that the focal spot blurring could be resolved and that the effect of the detector pixel size on the resolution was reduced [26]. Although the magnification was approximately constant during the measurements, the results show a slightly increasing magnification with increasing powers. As the source-detector distance is assumed to be constant during the measurements, the source-object distance must have changed. Figure 5.6c shows the different source-object distances. According to this figure, the source-object distance changes approximately 10 μm from the highest to the lowest magnification. It is possible that the change in source-object distance is related to the flat field correction performed between each measurement, where the sample is moved in and out of the detectors field of view.

Figures 5.7a-d show four comparisons between the measured projections of the cylindrical carbon steel sample and two simulated projections, for powers 10, 17, 23 and 30 W. One of the simulated projections uses a point source while the other is obtained by convoluting the point source projection with the optimized focal spot distribution. Although the point simulated projections are in good agreement with the measured projections, they can not explain the blurring at the penumbra. When the point simulated projections are convoluted with the optimized Gaussian focal spot distribution, a better fit between the simulated and measured projections can be observed in the

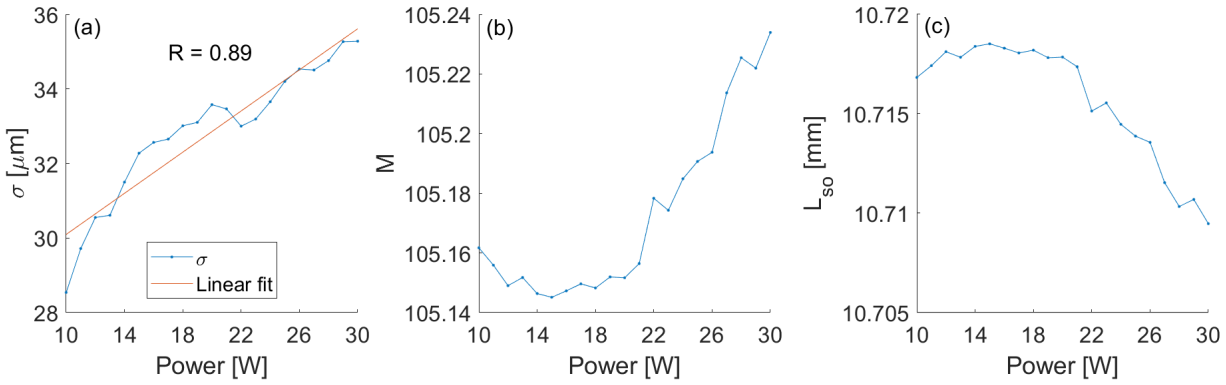

Figure 5.6: (a) Focal spot size given in σ, (b) magnification M and (c) source-object distance L_{so} as a function of power.

enhanced edge sections. Figure 5.7e presents the relative error between the measured and simulated projections. It is worth noting the overall increasing relative error for increasing powers. The primary region of interest in Figure 5.7e lies at the two edges of the sample, where a rapid increase in the relative errors can be observed. This is caused by the overestimated size of the Gaussian focal spot distributions, as seen in the enhanced edge sections of Figures 5.7a-d. Lastly, Figure 5.7f presents the Gaussian focal spot distributions for the mentioned powers. Except for powers, P = 17 W and P = 23 W, the focal spot distributions seem to increase with increasing powers.

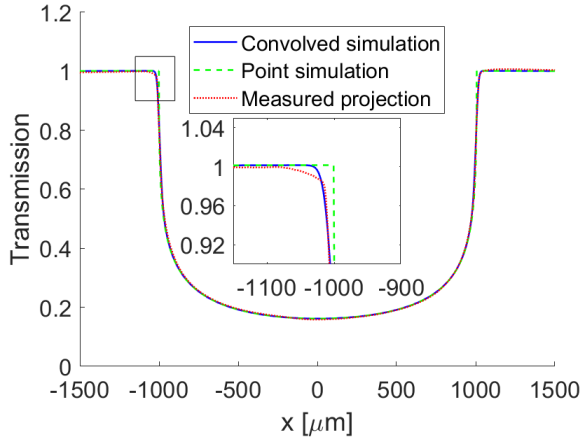

(a) P = 10 W.

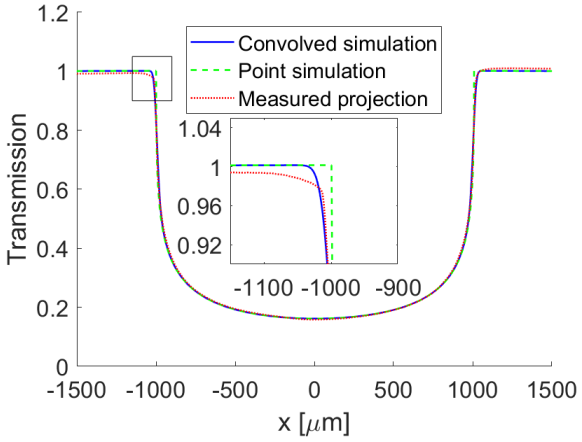

(b) P = 17 W.

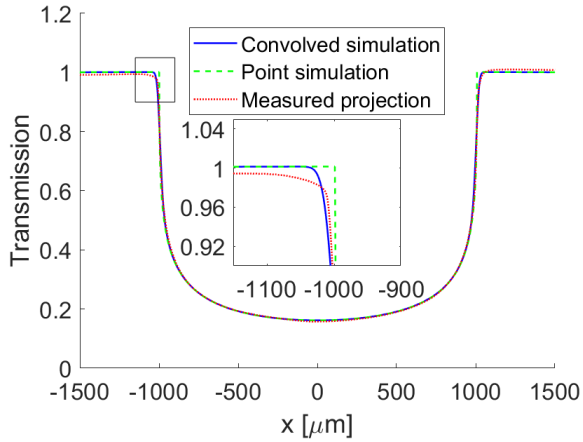

(c) P = 23 W.

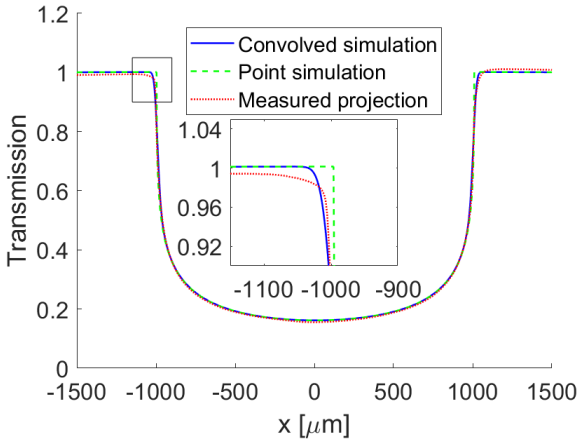

(d) P = 30 W.

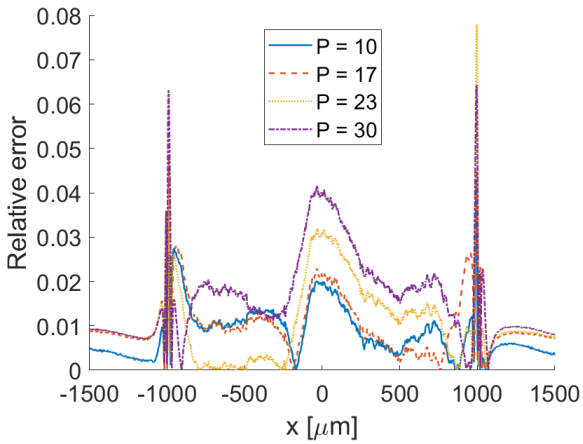

(e)

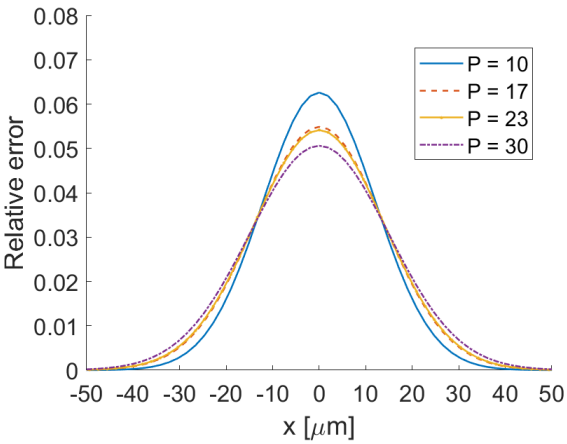

(f)

Figure 5.7: A comparison of the point and convoluted simulated to the measured data is given in (a)-(d). (e) Relative error between convoluted simulations and measured projections and (f) Gaussian focal spot distributions in (a)-(d).

5.4 Beam hardening in cylindrical samples

In this section simulations and measurements of three cylindrical samples are presented. Cross sections and accompanying horizontal profile plots going through the center of the cylinders are also presented.

The POM sample was measured using a tube voltage of 120 kV. Figure 5.8 presents cross sections of both measured and simulated tomograms of the sample. The simulated cross section seems to have a slightly higher degree of noise than the measured cross section and there is no presence of beam hardening in either of the reconstructed samples. Both assessments are supported by the horizontal profile plot in Figure 5.12a. The profile plot varies around a value of 1, showing no beam hardening artifacts. The standard deviation inside the cylindrical sample was computed, giving an attenuation value of 0.050 for the measured cross section and an attenuation value of 0.061 for the simulated cross section.

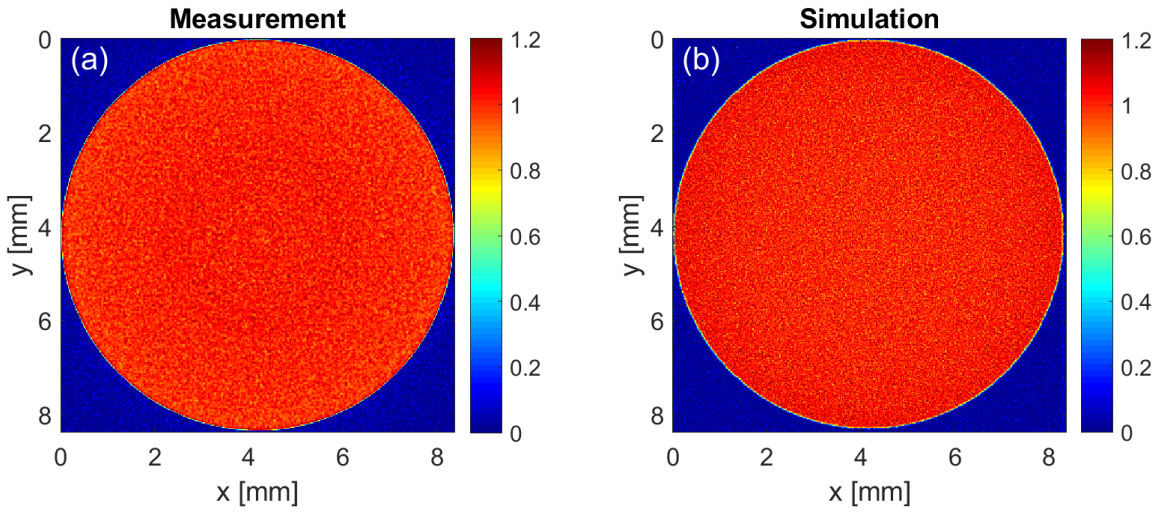

Figure 5.8: POM sample measured and simulated with a tube voltage of 120 kV.

The results from the Teflon sample using a tube voltage of 120 kV is presented in Figure 5.9, where Figure 5.9a shows the measured cross section while Figure 5.9b shows the simulated reconstructed cross section. Figure 5.12b shows the profile of the horizontal line going through the center of the sample. The simulated cross section and the profile plot show beam hardening in the form of a cupping artifact. The relative error of the average boundary value to the average center value is approximately 17 % in the simulated cross section. No beam hardening can be observed in the measured data.

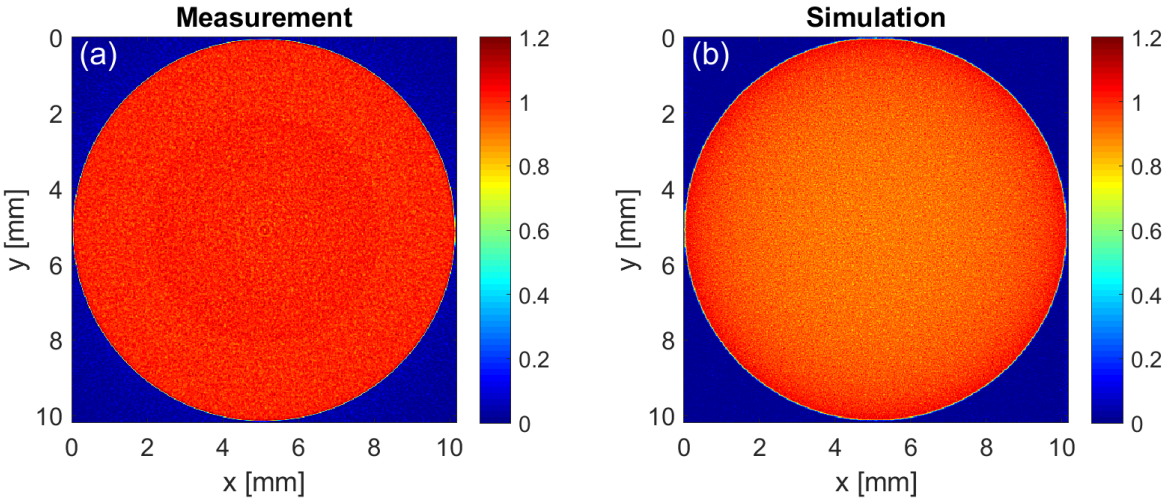

Figure 5.9: Teflon measured and simulated at a tube voltage of 120 kV

The measured and simulated cross sections of the Al sample are presented in Figures 5.10a and 5.10b, respectively, while the horizontal profile plot is presented in Figure 5.12c. Beam hardening can be observed in both the measured and simulated cross sections, however, the simulation shows a greater extent of beam hardening. The relative error of the average boundary value to the average center value is approximately 21 % in the measured cross section and around 31 % in the simulated cross section. Lastly, the observed noise in the profile plot seems to match well for the two reconstructed cross sections.

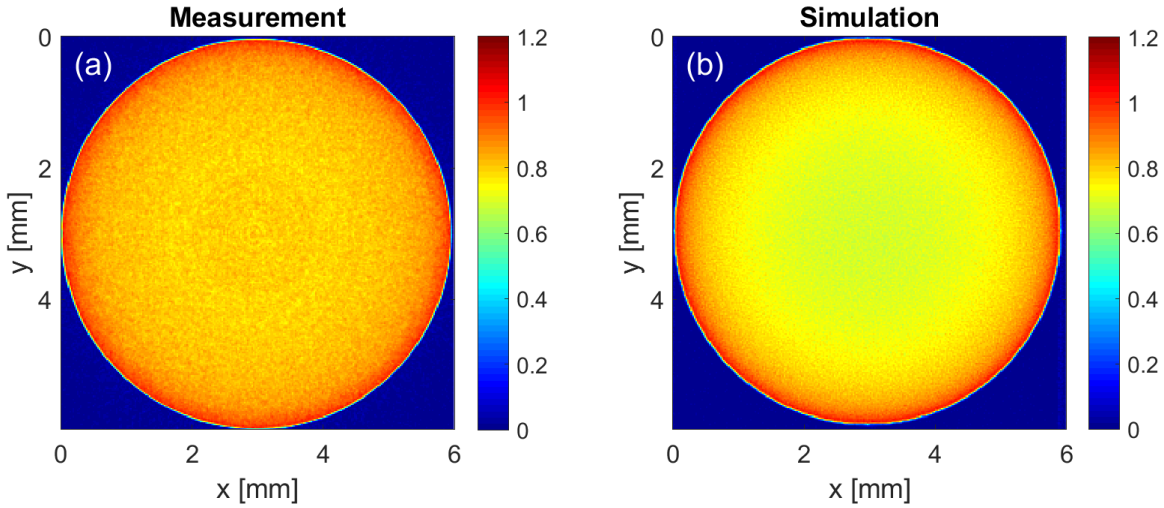

Figure 5.10: Measured and simulated sample of Al with a tube voltage of 120 kV.

Due to the beam hardening artifact, the Al sample was also measured and simulated using a 0.25

mm Cu filter keeping all other parameters the same. The results are presented in Figures 5.11a and 5.11b for the measured and simulated tomograms, respectively. Here, ring artifacts observed as concentric rings around the axis of rotation is present in the measured tomogram. One can further observe that both tomograms are now essentially free of the cupping artifact, demonstrating that filtering the source spectrum may effectively remove cupping artifacts in tomograms. A common consequence of spectrum filtration is that the noise increases in the projections as fewer photons reach the detector. However, the noise may normally be reduced by increasing the exposure time. Figure 5.12d shows the horizontal profile plot through the center of the sample. The standard deviation inside the cylindrical sample was computed, giving an attenuation value of 0.042 for the measured tomogram and 0.045 for the simulated tomogram. By comparing the horizontal profile plot with the profile plot in Figure 5.12c, one can confirm that the noise has increased as expected.

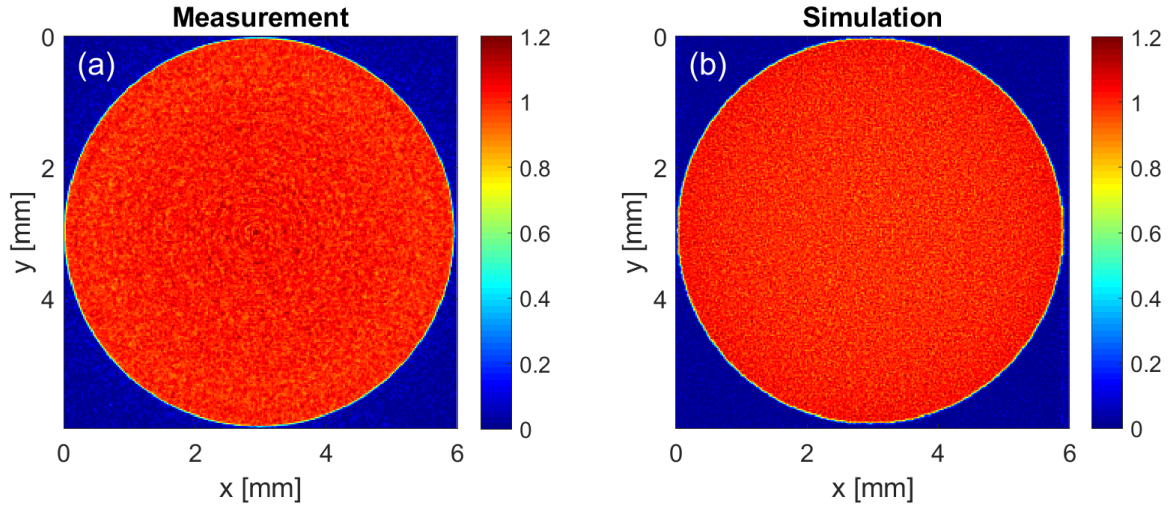

Figure 5.11: Al sample measured and simulated with a 0.25 mm Cu filter.

The transition between the surrounding air and the samples in this section is sharp and without any extensive blurring. This is due to the use of ramp filters in the reconstruction algorithm, which does not suppress any high frequency noise. In the simulations, a Ram-Lak ramp filter was used to reconstruct the sample. The experimental data uses an unknown implementation of the ramp filter. The consequence of using ramp filters is that they enhance any noise present in the projections. While low-pass filters such as Hann or Hamming filters may be used in the reconstruction algorithms to suppress noise in the reconstructed tomograms, they will also blur the transition between materials due to the suppression of high-frequency components. This blurring effectively reduces the resolution in the tomograms. It can therefore be argued that the choice of reconstruction filter depends primarily on the sample to be imaged. For high-resolution imaging a ramp filter is preferred, while a Hann or Hamming filter may be used for samples where low noise is important.

A discrepancy in beam hardening was observed between the simulated and the measured tomograms in this section. This discrepancy is caused by discrepancies in the projections of the sample, implying that the parameter $\eta(V)$ does not perform as intended. However, without the parameter the beam hardening would be much more severe in the simulated tomograms due to the additional path length through the samples. It is paramount that the model for the source spectrum is improved in future work.

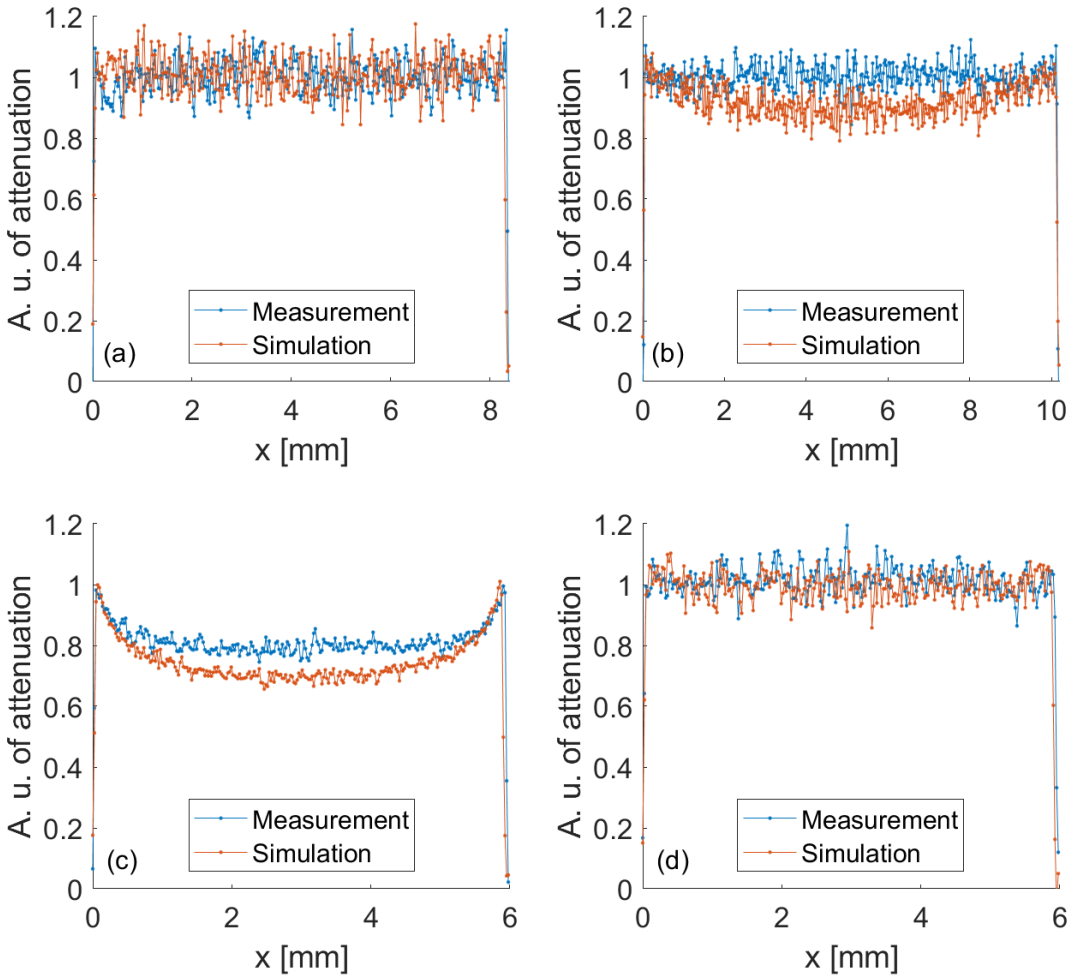

Figure 5.12: Horizontal profile plots of the POM, teflon and Al samples going through the center of their respective cross sections. (a) POM measured at 120 kV, (b) Teflon measured at 120 kV, (c) Al sample measured at 120 kV, and (d) Al measured at 120 kV with a 0.25 mm Cu filter.

5.5 Polychromatic CT simulations of layered Ni-Sn samples

A sample consisting of Ni and Ni_3Sn_2 has been simulated to analyze the effect of focal spot blurring in tomograms. More specifically, we are interested in knowing what the layer thickness of Ni_3Sn_2 must be in order to resolve it in the reconstructed tomograms. Figure 5.13a presents a simulation of the reconstructed cross section with an ideal source and without noise, denoted the ideal simulation. Beam hardening can be observed in the sample, as the attenuation coefficients are higher at the edges of the Ni and Ni_3Sn_2 layers and decreases towards the center. Although beam hardening can be observed in the tomogram, the two materials Ni and Ni_3Sn_2 can still be clearly distinguished. Figure 5.13b presents the simulated cross section where the projections have been convoluted with the appropriate focal spot size as determined in section 5.3. In this setup the boundaries that could be observed in the ideal simulation are blurred out due to the source size, making discrimination of the two materials more difficult. Figure 5.13c presents the cross section with both a finite focal spot size and Poisson noise, denoted the full simulation. This figure should in principle illustrate what the reconstructed cross section of a real CT measurement would yield. Finally, Figure 5.13d, which is the full simulation subtracted from the ideal simulation, clearly illustrates the blurring effect of the focal spot size on the boundaries between different materials in the cross sections. Four horizontal bright lines can be observed, revealing the locations of the material boundaries.

The effect of Poisson noise and focal spot blurring may be better illustrated through profile plots. Figures 5.14a and 5.14b present profiles along the layer normal through the center and close to the boundary, respectively, for both the simulation and the measurement. The edges around the Ni layer are clearly blurred out in the full simulation, while the ideal simulation shows a ledge around 700 μm and 800 μm. Both figures show that the full simulation reaches the value of the ideal simulation, indicating that the full simulation can fully resolve the Ni_3Sn_2 layer. Here the layer thickness is 16 pixels with 4 μm per pixel, indicating that the Ni_3Sn_2 phase can not be thinner than 64 μm in order to resolve it in the tomograms. Decreasing the layer thickness further yields a lower attenuation coefficient in the full simulation than in the ideal simulation, and the layer might therefore be confused with other phases.

Figure 5.14c shows the profiles along the layers for the two materials in the sample of the full simulation, while Figure 5.14d shows the same profiles for the ideal simulation. Here, beam hardening is present even though the source spectrum was filtered with a 1.00 mm Cu filter. The relative error of the boundary to the center in the two Ni_3Sn_2 profile plots is approximately 18 %. The boundaries of both Ni and Ni_3Sn_2 are shown to be blurred in the full simulation in Figure 5.14c due to the focal spot blurring.

The beam hardening can be alleviated by replacing the 1.00 mm Cu filter with 1.00 mm Ag filter.

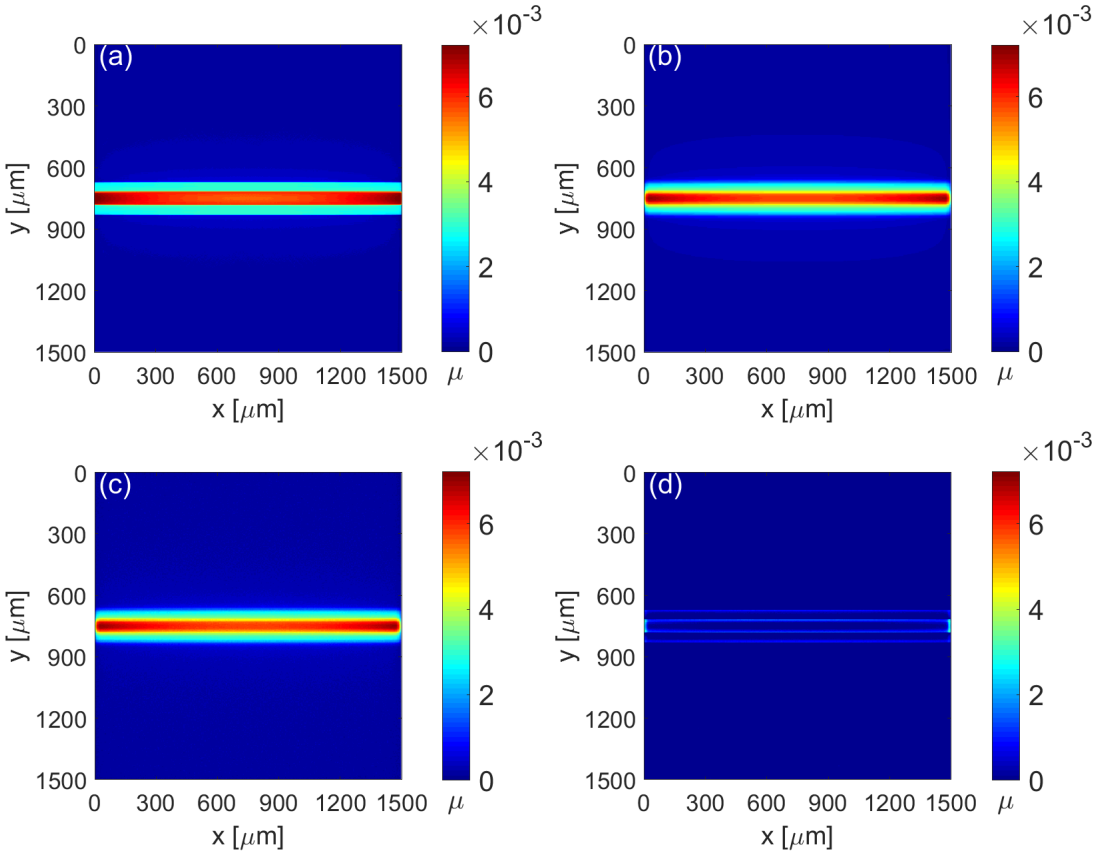

Figure 5.13: Simulation of the Ni-Sn sample with a Ni_3Sn_2 layer thickness of 64 μm using a 0.25 mm Cu filter. (a) shows the cross section with an ideal source and without noise, (b) shows the cross section using an appropriate focal spot size, (c) shows the full simulation with both a finite sized focal spot size and Poisson noise. (d) shows the result of subtracting (c) from (a), clearly depicting the effect of the focal spot size.

This is simulated in Figure 5.15, keeping all other parameters constant. The ideal simulation in Figure 5.15a shows less beam hardening in the Ni and Ni_3Sn_2 layers, however, inspecting the full simulation in Figure 5.15 reveals that the noise has increased.

The profile plots along the layer normal in Figures 5.16a-b show more variations in the reconstructed attenuation coefficients. Figures 5.16c-d show the profile plots along the layers of the two materials in the full and ideal simulations, respectively. The relative error between the boundary and the center of the ideal profile plot of Ni_3Sn_2 is approximately 12 %, a difference of 6 percentage points compared to the 1.00 mm Cu filter. The consequence is a significant increase in noise. It is possible to reduce the noise by increasing the exposure time. If, however, the exposure time is maximized, one must consider whether the reduction in beam hardening can justify the additional

noise. The additional noise would inhibit the ability to distinguish materials with similar attenuation coefficients such as Ni-Sn phases. However, if the sample is homogeneous or the materials are easily distinguishable, such as the Ni and Ni_3Sn_2, the additional noise could be justified.

By decreasing the current from 100 μA to 10 μA the focal spot size also decreases, providing a better resolution. Figure 5.17a shows the ideal simulation of the layered Ni-Sn sample using a 1.00 mm Cu filter and a layer thickness of 56 μm for the Ni_3Sn_2 phase. Figure 5.17b shows the simulation where the projections were convoluted with the focal spot size and Poisson noise was added to the projections, showing no apparent difference compared to Figure 5.13c.

The vertical profile plots in Figures 5.18a and 5.18b show increased noise in the Si layers. Although the noise has increased, the resolution has also increased from 64 μm using a current of 100 μA to 56 μm with a current of 10 μA.

As the focal spot size is considerably larger than what Nikon guarantees for a power of 1.8 W, a simulation using a focal spot size of 3 μm and a current of 10 μA has been performed. By comparing the full simulation and the ideal simulation in Figure 5.17, it can be observed that the focal spot size has no impact on the resolution in the full simulation. The layer thickness is 16 μm, and here the physical resolution is limited only by the reconstruction algorithm. By reducing the pixel size, blurring due to the focal spot size would eventually effect the physical resolution again.

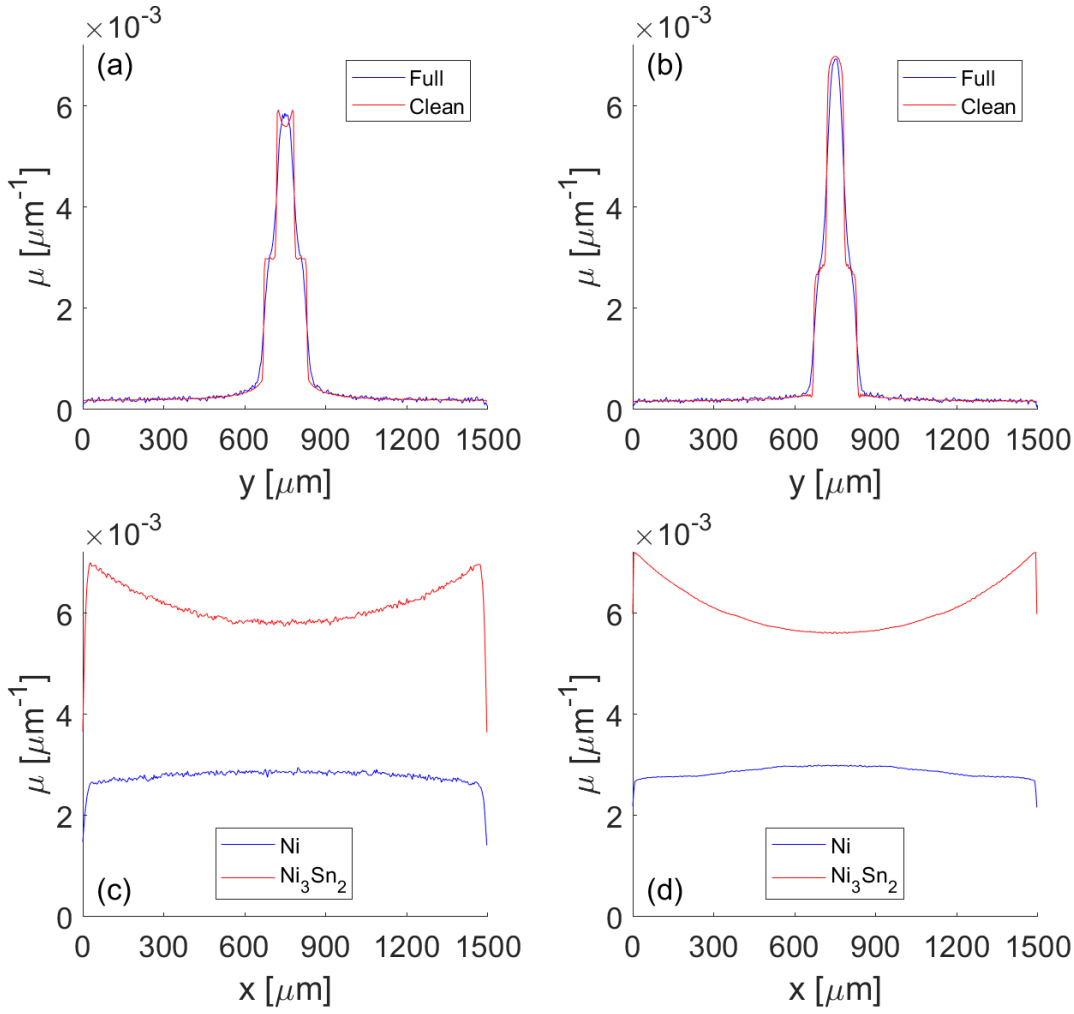

Figure 5.14: Profile plots along the layers and perpendicular to the layers of the Ni-Sn sample. The Ni_3Sn_2 layer thickness was 64 μm and a 0.25 mm Cu filter was used. (a) and (b) show the vertical profiles going through the center and the boundary, respectively, while (c) and (d) present the profiles going through the center of the phases in the sample for the full and ideal reconstructed cross sections, respectively.

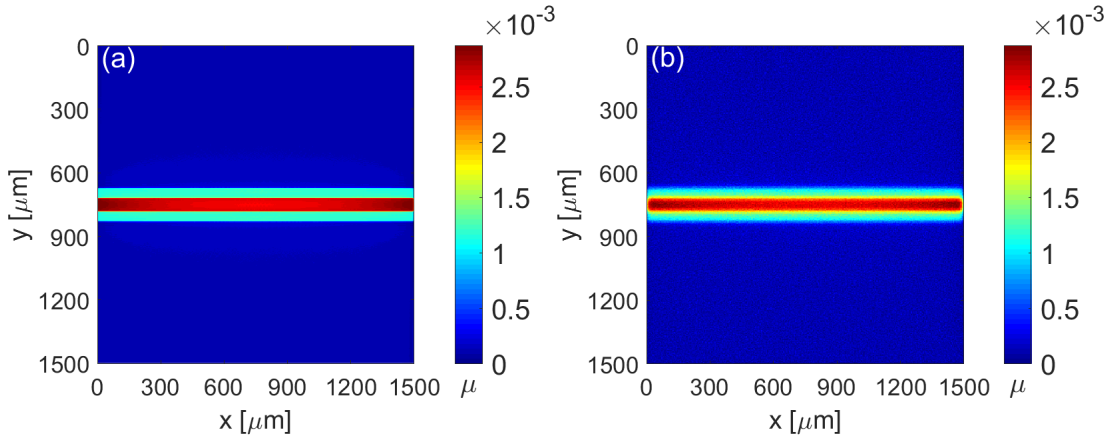

Figure 5.15: Simulations of the Ni-Sn sample with a Ni_3Sn_2 layer thickness of 64 μm using a 1.00 mm Ag filter. (a) ideal simulation of the cross section without a focal spot size and noise. (b) Full simulation of the cross section with focal spot size and noise.

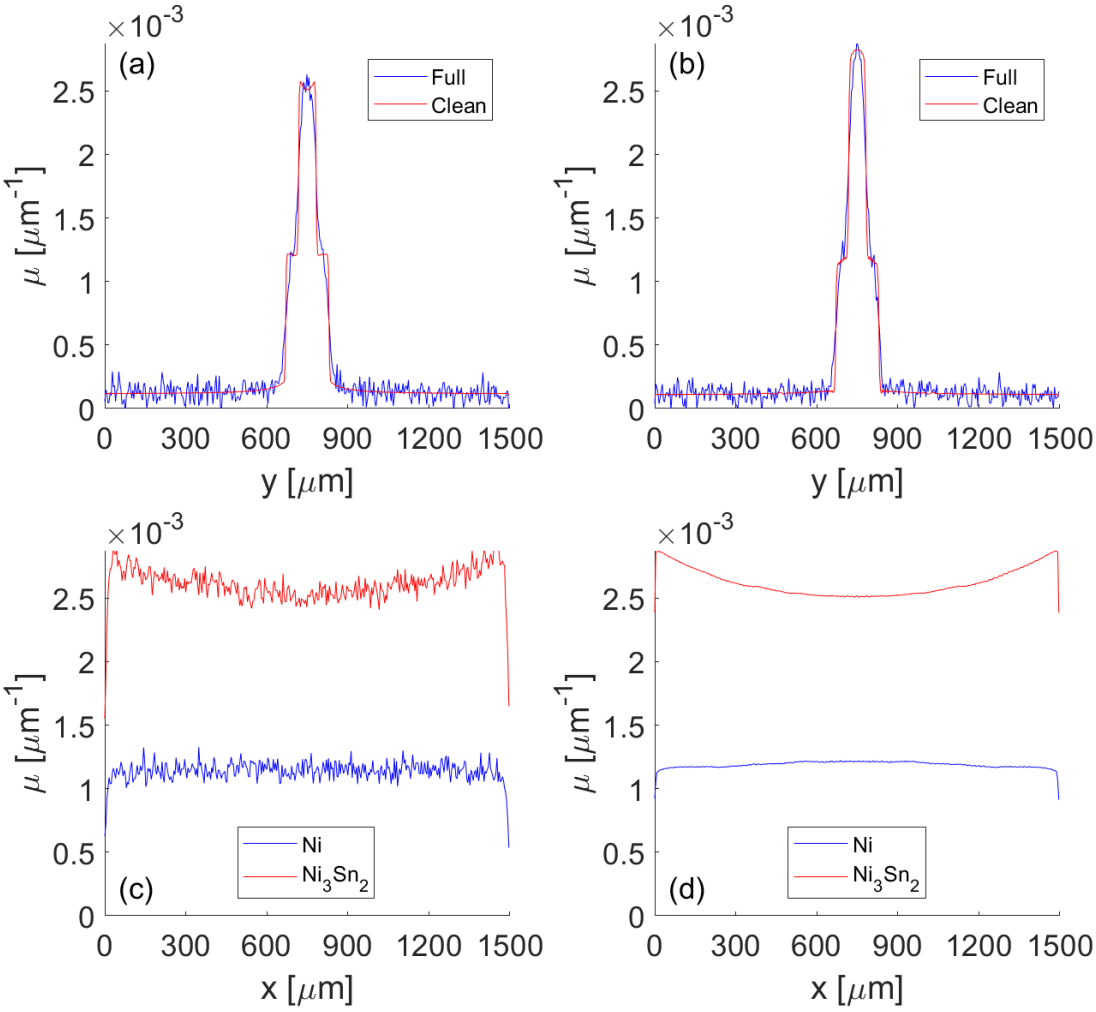

Figure 5.16: Profile plots of the smaller Ni-Sn sample with a Ni_3Sn_2 layer thickness of 64 μm and a 1.00 mm Ag filter. (a) and (b) shows the profiles along the layer normal of the sample through the center and the boundary, respectively. (c) and (d) shows the profiles along the layers of the different material layers in the full and ideal reconstructed cross sections, respectively.

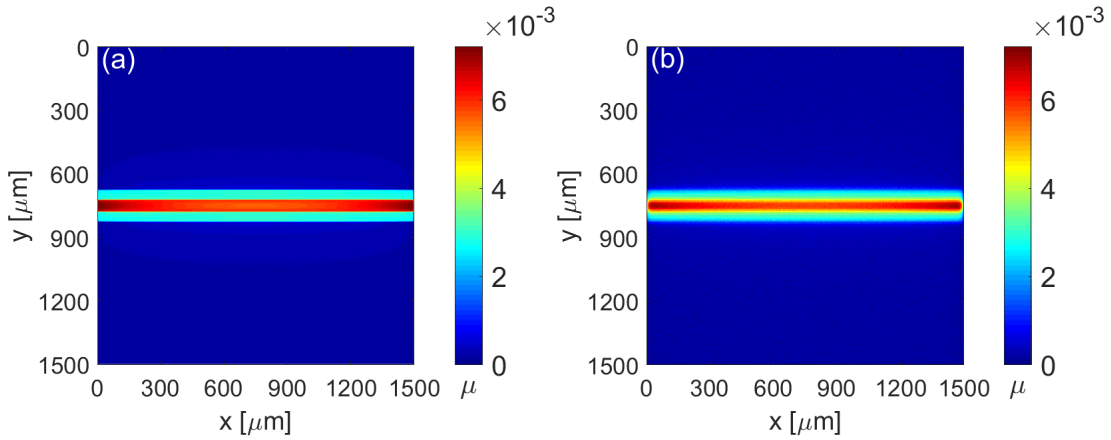

Figure 5.17: Simulation of the Ni-Sn sample with a Ni_3Sn_2 layer thickness of 56 μm and a 1.00 mm Cu filter. (a) Ideal simulation. (b) Full simulation with the focal spot size and applied Poisson noise.

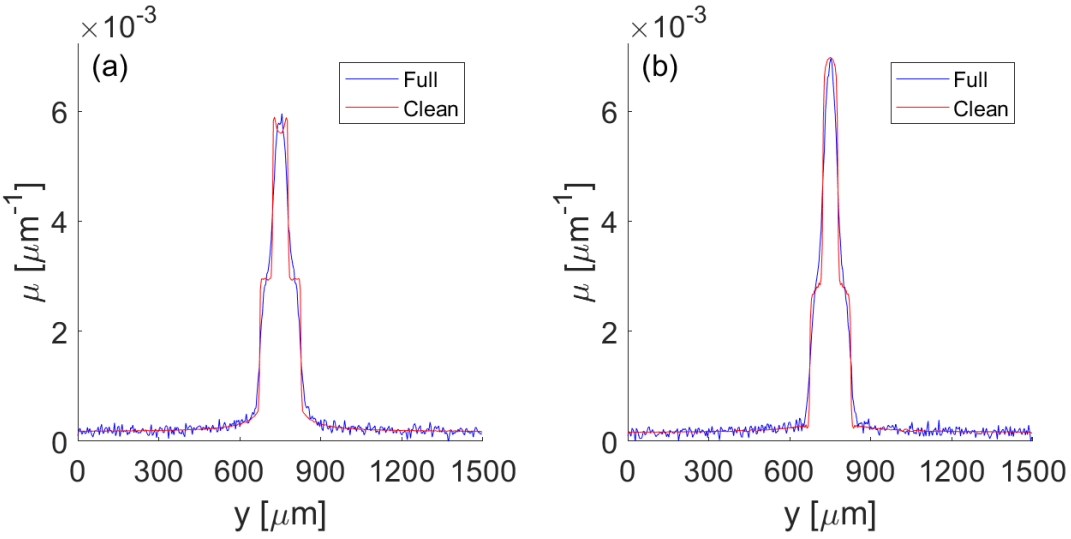

Figure 5.18: Profiles along the layer normal of the reconstructed cross section of the Ni-Sn sample with a pixel size of 4 μm and a Ni_3Sn_2 layer thickness of 56 μm. (a) profile through the center of the sample, (b) profile through the edge of the sample.

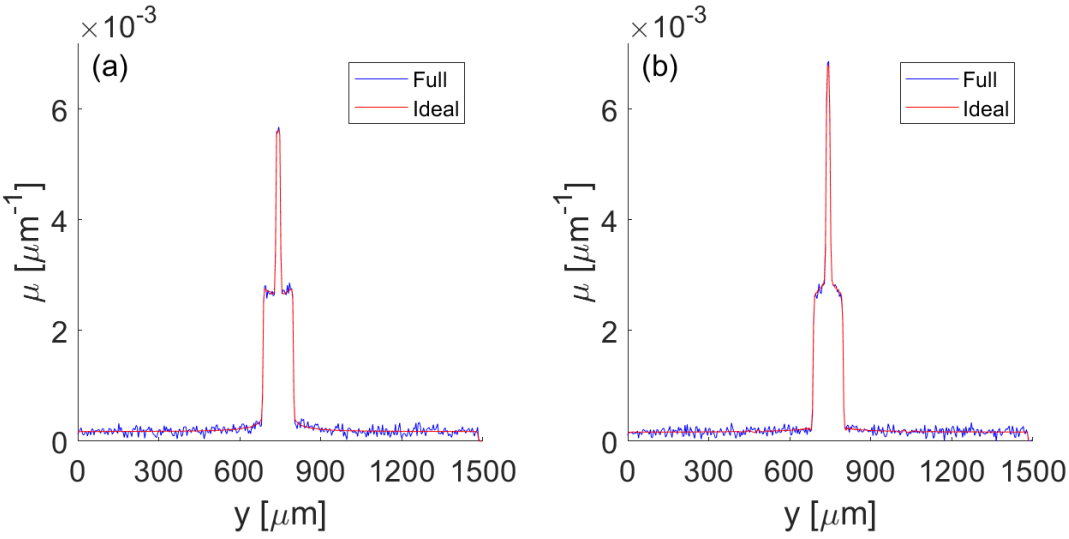

Figure 5.19: Profiles along the layer normal of the reconstructed cross section of the Ni-Sn sample with a pixel size of 4 μm and a Ni_3Sn_2 layer thickness of 16 μm. A 3 μm focal spot size was used. (a) profile through the center of the sample, (b) profile through the edge of the sample.

5.6 Polychromatic CT measurement of Au-Sn SLID sample

The Au-Sn SLID sample was measured using the Nikon CT instrument. Figure 5.20a shows the entire reconstructed Au-Sn SLID sample rendered in three dimensions using an isosurface with an isovalue of 114. The figure depicts the entire reconstructed sample, including a crack on top of the sample. Figure 5.20b is a three dimensional rendering showing the interior of the sample, denoting the PZT layer, WC layer and the Au-Sn bond layer.

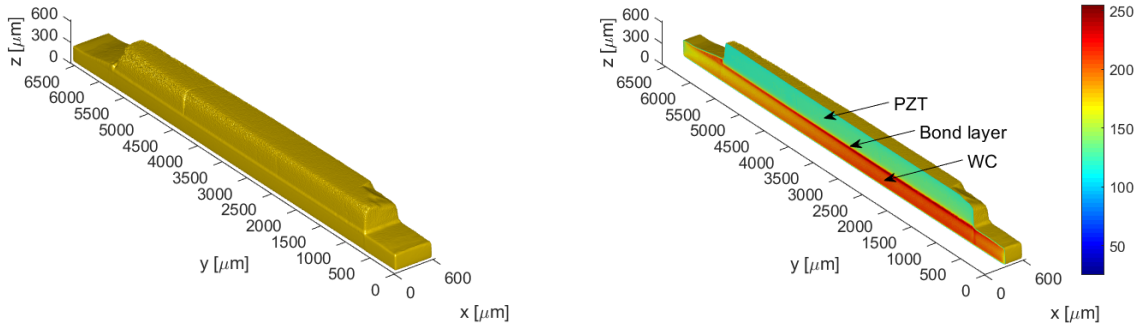

(a) **(b)**

Figure 5.20: Isosurface renderings of the experimentally measured Au-Sn SLID sample. (a) Whole sample, (b) cutaway view of the sample showing the material layers.

Figures 5.21a-c show three cross sections, namely the xy, yz and xz cross sections of the sample. The xy cross section shows features in the range 1000 μm to 2000 μm in the y-direction, however, these features are not related to the bond. The yz cross section shows a decreasing attenuation value for increasing y, possibly due to the anode heel effect. Moreover, the xz cross section clearly depicts the bond layer around $z = 250$ μm, shown as a deep red color in the cross section. Both the WC and PZT parts of the sample show beam hardening artifacts along the edges.

In order to confirm that the decreasing attenuation values for increasing y values in Figure 5.21b is an artifact from the CT measurement, the Au-Sn SLID sample was measured two additional times. The first of these two additional measurements was performed with the y-direction placed normal to the sample stage. The second of these two additional measurements was performed by rotating the sample 180 degrees in the xy plane. The reconstructed yz cross sections of the two CT measurements are presented in Figures 5.22a and 5.22b for the first and second additional measurement, respectively. Observing the attenuation values along the y direction one can see that the attenuation drops for increasing y values in both cases. This supports the claim that the attenuation drop is an artifact of the CT measurement rather than a consequence of the sample itself. One possible explanation for this artifact might be the source filtration due to the anode heel effect in the X-ray source, as explained in section 2.9.5.

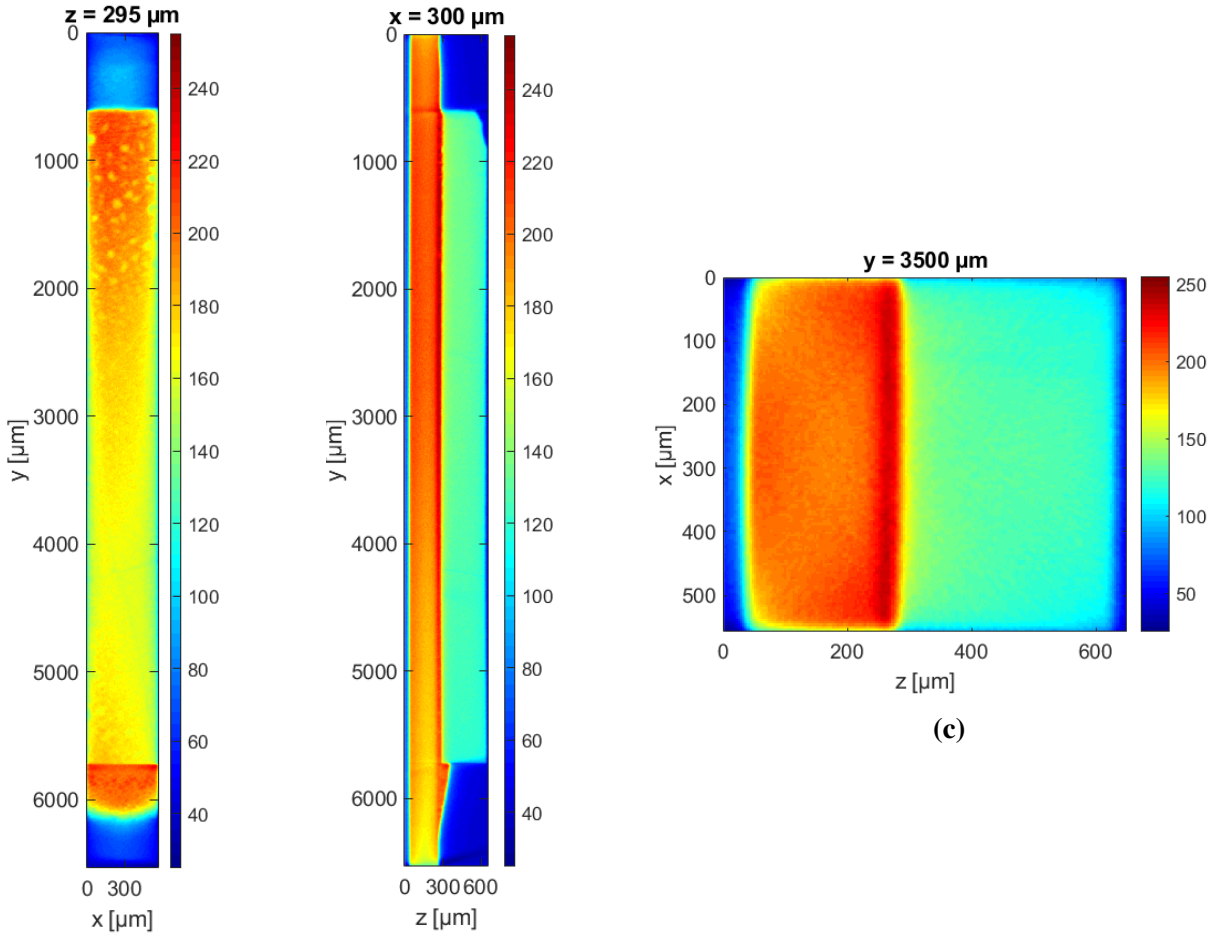

(a) **(b)** **(c)**

Figure 5.21: Reconstructed cross sections of the Au-Sn SLID sample. (a) xy cross section at z=295 μm, which is at the boundary between the PZT material and the Au layer. (b) yz cross section and (c) xz cross section.

Figure 5.23 presents eight cross sections of the bond layer. In these cross sections one can observe features in the bond layer, which are due to the presence of different phases. Notably, the features seem to propagate through the entire bond layer.

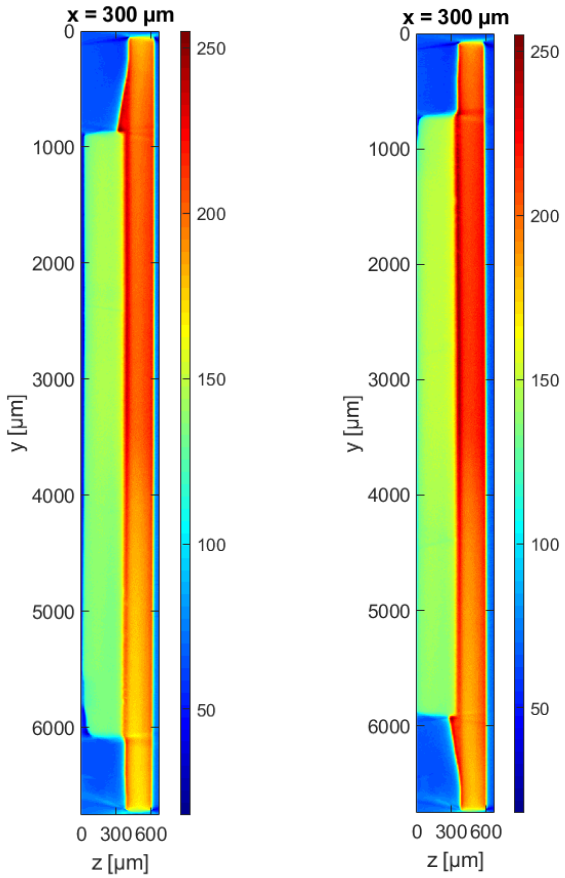

(a) **(b)**

Figure 5.22: Two *yz* cross sections of the Au-Sn SLID sample from two CT measurements with two different orientations of the sample. (a) Upright position of the sample, (b) sample rotated 180 degrees and mirrored in order to compare the two cross sections. Both cross sections show an increase in attenuation value in the WC part for increasing y values, supporting the claim that this is an artifact of the measurement.

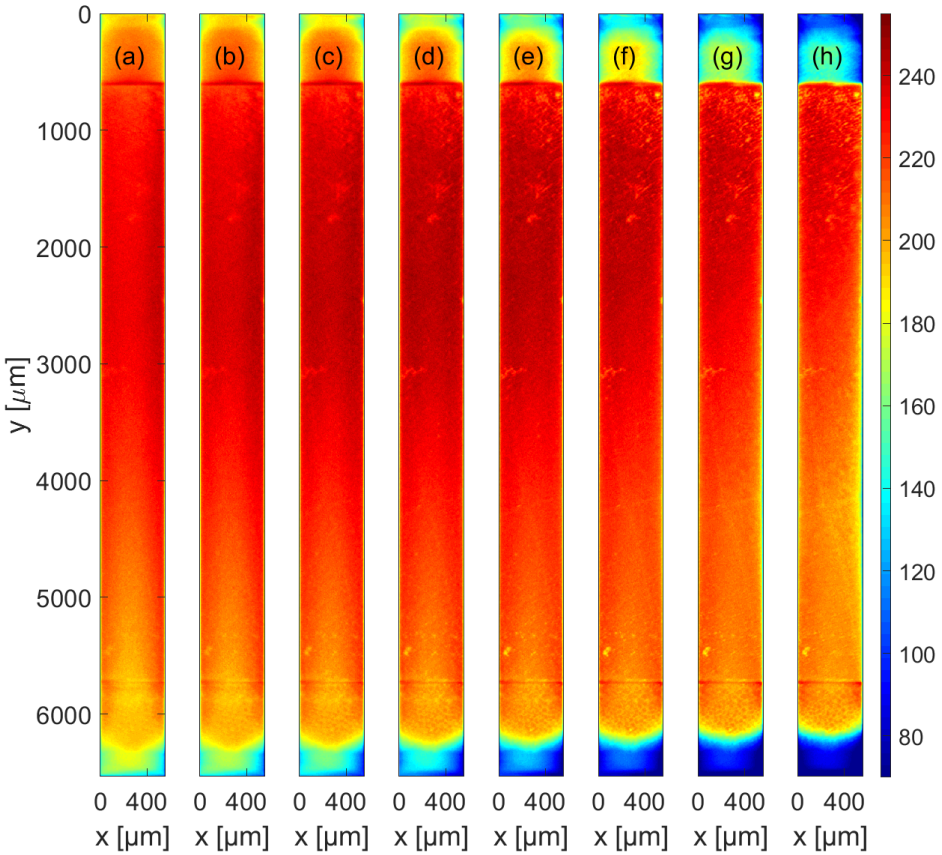

Figure 5.23: Multiple cross sections of the Au-Sn SLID sample showing the bond layer of the sample. Here, Δz is equal to the pixel size showing each reconstructed tomogram of the bond layer. Heterogeneous features can be observed in the bond, possibly due to the presence of two distinguishable phases.

5.7 Synchrotron CT measurement of Ni-Sn SLID sample

The CT measurement of the Ni-Sn SLID sample performed at the synchrotron was conducted with a monochromatic and partially coherent X-ray source. Figure 5.24a shows the linear attenuation coefficients for the different possible materials in the Ni-Sn SLID sample. The figure shows that the Si attenuation coefficient is approximately one order of magnitude lower than Ni and two orders of magnitude lower than Sn. Figure 5.24b reveals that the attenuation coefficients of the Ni-Sn phases are similar, making it difficult to distinguish between the different phases using absorption contrast. The figure emphasizes the energy used in the synchrotron CT experiment

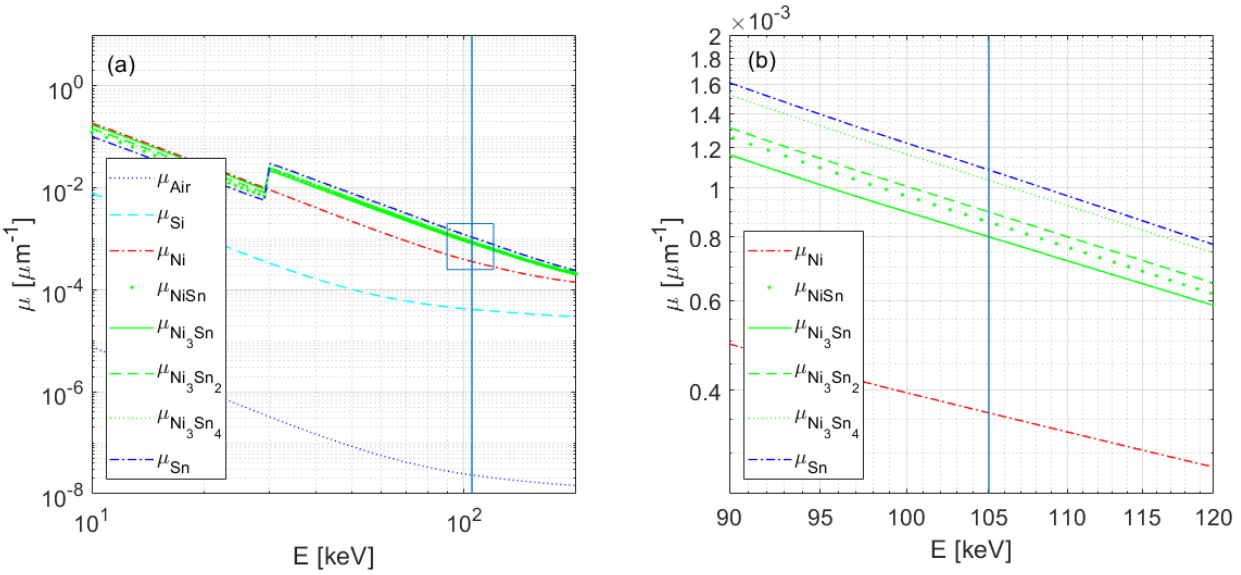

Figure 5.24: Attenuation coefficients for the materials in the Ni-Sn sample. (a) Attenuation coefficients, (b) closer look at the attenuation coefficients for the Ni, Sn and Ni-Sn phases. Note that the attenuation of Sn and Ni-Sn phases are relatively close, while Ni has a relatively lower attenuation coefficient than the Ni-Sn phases. 105 keV is emphasized as this is the energy used in the synchrotron CT experiment.

Figure 5.25a presents a cross section of the the bond layer in the Ni-Sn SLID sample with four horizontal and four vertical lines. These lines show where the xz and yz planes in Figures 5.25b and 5.25c cross the bonding layer. The colormap ranges from 0 to 255 in the three figures, where higher numbers are linked to materials with higher attenuation. The contrast in Figure 5.25a suggests that there are primarily two major structures in the bond layer, one structure with an attenuation value of around 100-125 and another with an attenuation ranging from 165-225. Figure 5.26c-f shows that the high attenuation structure extends approximately four voxels in the z-direction giving a total thickness of 9 μm. The first two and the last two images, Figures 5.26a-b and 5.26g-h, show less features as the bond cross sections are at the boundary of the bond layer, indicating that the

low attenuating structure surrounds the high attenuating structure. This is also supported by the cross sections presented in Figures 5.25b and 5.25c.

An xz cross section of the reconstructed Ni-Sn SLID sample is presented in Figure 5.27a, showing the surrounding air as well as the bonding layer sandwiched between the two Si wafers. The Figure is represented with 8-bit numbers with higher numbers representing materials with higher attenuation. A simulation of the CT measurement using monochromatic and incoherent radiation with white Gaussian additive noise has also been computed. The simulated reconstruction of the sample is presented in Figure 5.27b, with the aforementioned assumed structure of the sample given in Table 3.4. The simulated bond layer is divided into five sections, where three of the sections contain Ni_3Sn_2, one section contains air and one section contains Ni. In the figure, the Ni_3Sn_2 sections are indicated by the numbers 1, 3 and 5, while the air and Ni sections are respectively indicated by 2 and 4.

There are at least two differences between the measured and simulated reconstructions in Figure 5.27. First, dark and bright bands can be observed in the measured reconstructed sample. Such dark bands are often attributed to photon starvation in ordinary CT measurements with absorption contrast [5]. Due to the absence of these artifacts in the simulations, it is assumed that they are due to the additional phase contrast in the measured sample.

Second, the edges in Figure 5.27(a) are clearly enhanced at the boundary between the Si layers and the air. This is due to the combined contribution from phase contrast and absorption contrast in the measured projections. Although the phase contrast has been converted to an attenuation-like absorption contrast through equation (2.23), some residual phase contrast fringes or contrast blurring can still be observed in the reconstructed sample. The explanation is that the sample used is heterogeneous rather than homogeneous, violating one of the assumptions used in deriving the results in equation (2.23). The edge-enhanced phase contrast can not be observed in the simulation as the model used in the simulations is based on pure absorption contrast, which provide no phase information.

The Paganin approximation in equation (2.23) depends on the ratio δ/β in the refractive index, as well as the attenuation coefficient μ, of the assumed homogeneous sample. Changing these constants in the algorithm could reduce some of the edge-enhanced contrast between the Si and the surrounding air. However, this may result in increased edge-enhanced phase contrast between Ni, Sn and Ni-Sn phases. It is therefore assumed that the constants, δ and β, have been optimized such that the edge-enhanced phase contrast is minimized in the bond layer materials.

Figure 5.28a shows a profile plot normal to the bond layer for $x = 2205$ μm. The values for the Si in the measured profile are consistent with the simulated line profile. Furthermore, the enhanced plot

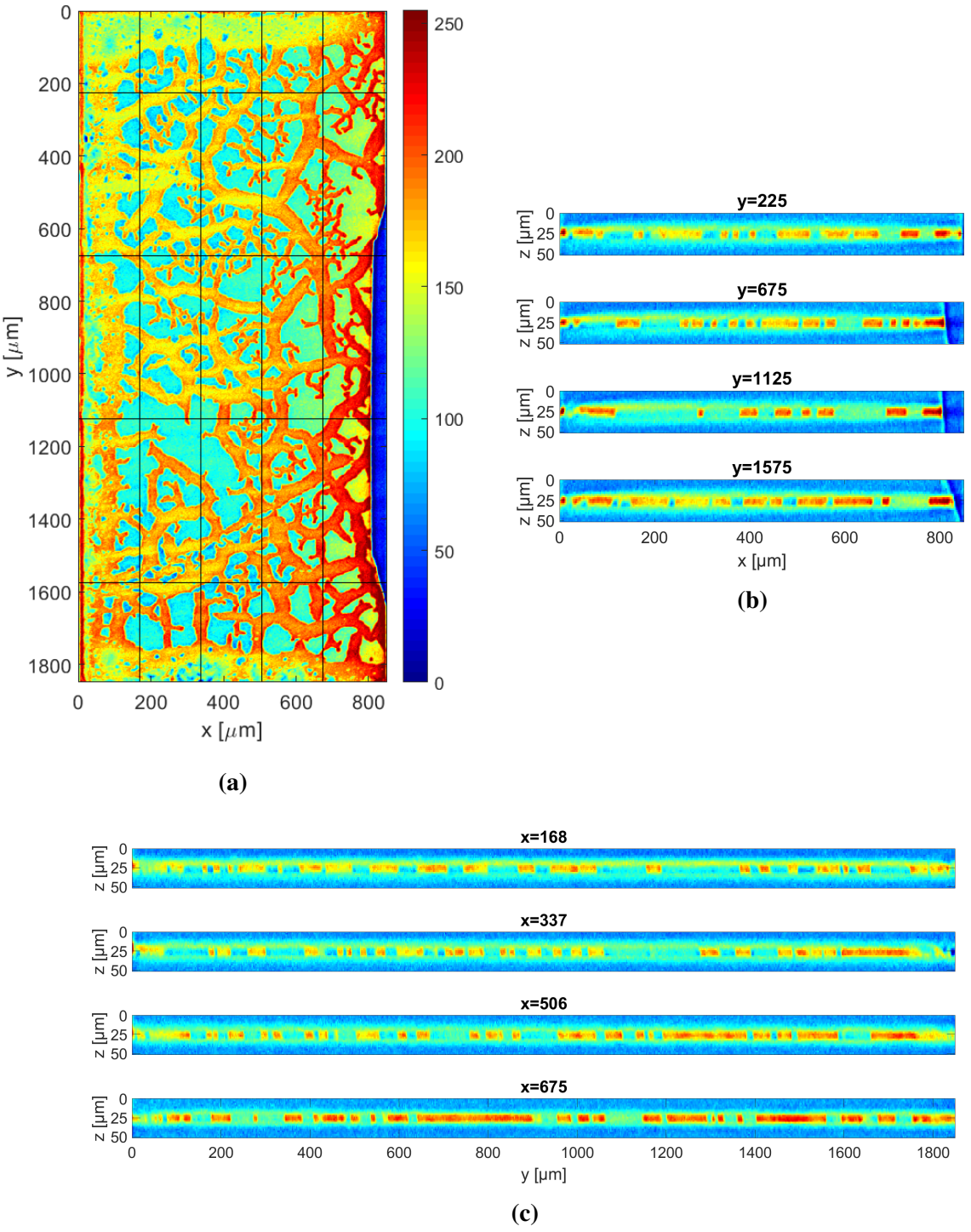

Figure 5.25: Cross sections of the Ni-Sn region of the sample. (a) xy cross section showing the structures and the lines which the cross sections in (b) and (c) goes through. (b) xz cross sections, and (c) yz cross sections. The range is 0 to 255 in the figures, and (b) and (c) are stretched in the z direction in order to better resolve the structure.

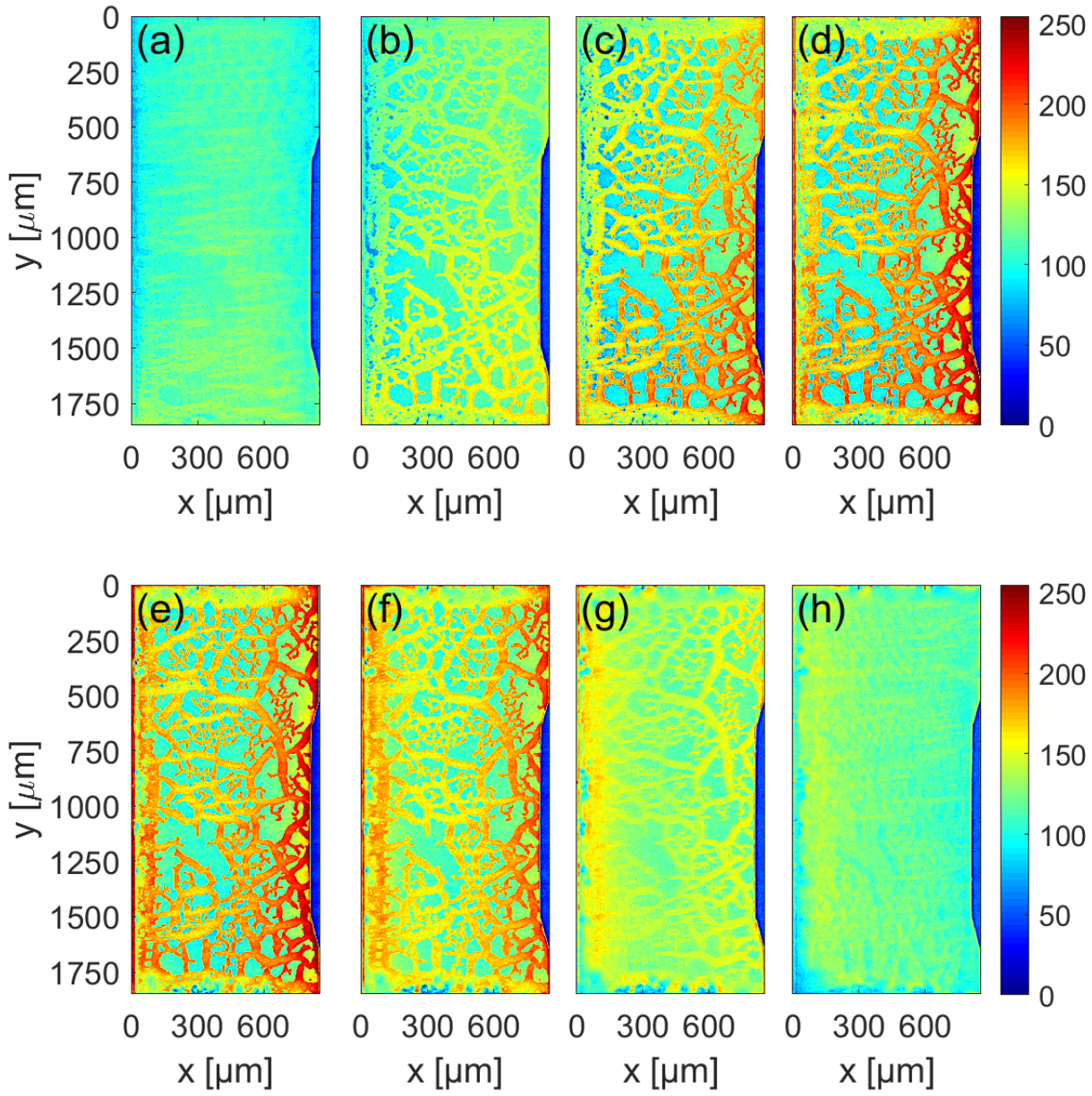

Figure 5.26: Xy cross sections of the Ni-Sn sample. Each cross section is shifted 2.25 μm in the sample.

of the bond layer in Figure 5.28a shows a good fit between the simulated and measured samples, implying that parts of the high-attenuating structure consist of the phase Ni_3Sn_2.

Figure 5.28b presents a horizontal line profile going through the center of the bond layer for both the measured and the simulated cross sections in Figure 5.27. The aforementioned sections are denoted by the same numbers 1 to 5. The profile plot shows that the simulated Ni region, section 4 in the profile plot, has an attenuation value comparable to the experimentally measured values,

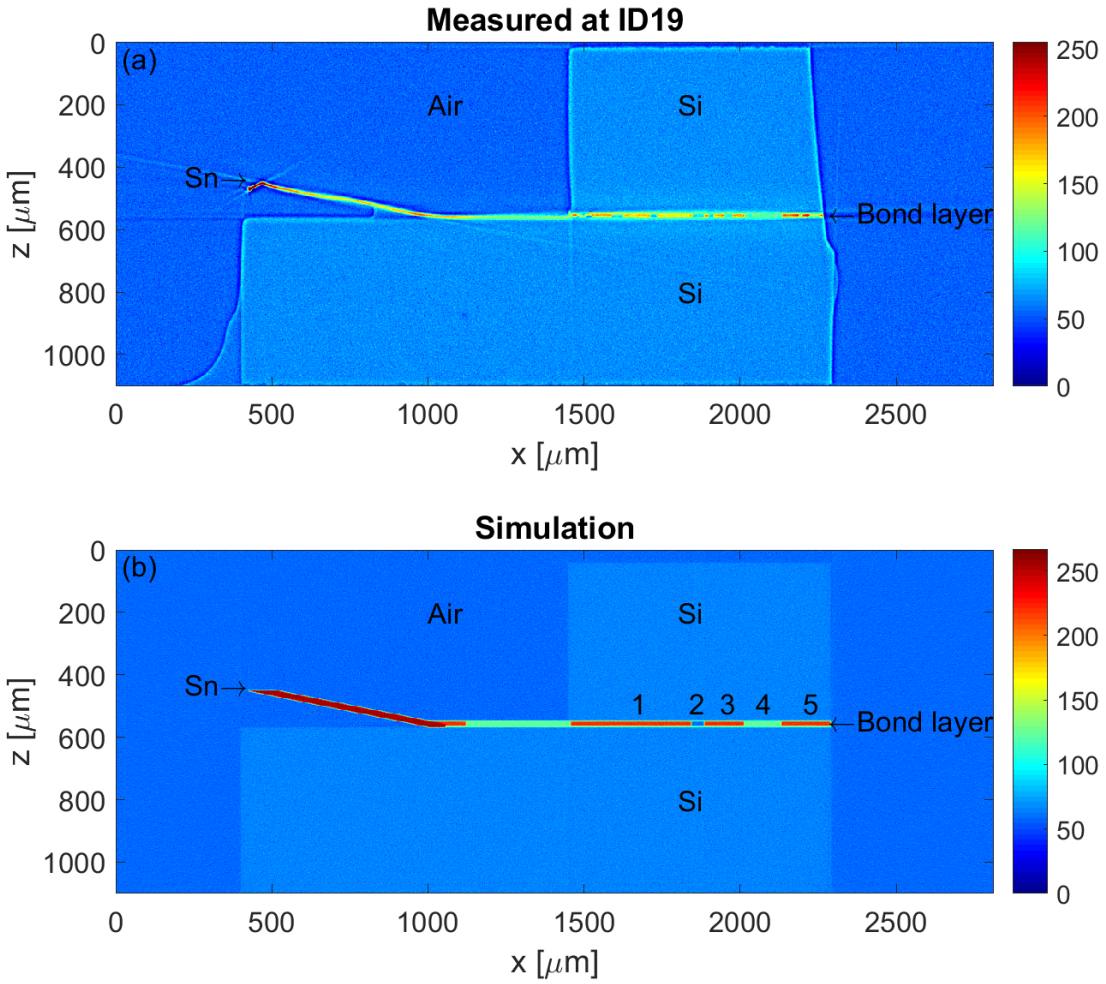

Figure 5.27: Xz cross sections of the measured and simulated sample showing the surrounding air, the Si layers and the bond layer. Note the edge-enhanced phase contrast between air and Si.

indicating that attenuation values around 125 consists of Ni in the measured data set. Several other sections in the measured profile plot display similar attenuation values. Most of them show an attenuation value that is slightly lower, usually between 100 to 125. It is possible that these sections contain Ni with a distribution of several air pockets that are smaller than or similar in size to the voxel size, effectively lowering the observed attenuation value. This is also supported by analyzing the simulated air pocket in section 2, which shows a lower attenuation value than any other point in the measured profile plot in the bond layer. The distribution of air pockets in the center of the bond layer has been reported by Tollefsen et. al. [13]. This gives good reasons to believe that the lower attenuation structure of the two major structures in the bond layer consists of primarily Ni with a distribution of air pockets.

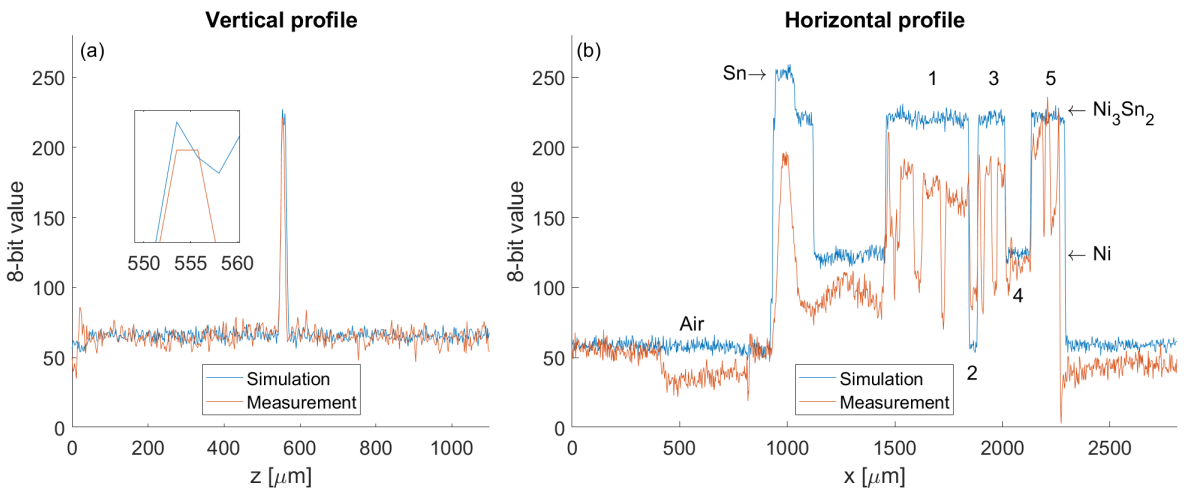

Figure 5.28: Horizontal and vertical profiles of the measured and simulated sample. (a) Profile plot as a function of z for $x = 2205$ μm. (b) Profile plot going through the center of the bond layer.

The results presented here indicate that there is a highly attenuating phase that partially consists of Ni_3Sn_2 and a lower attenuating structure consisting of Ni with a distribution of air pockets. The analysis depends on the scaling of the simulations. The value of Sn was assumed to be 254, which is reasonable as Sn is the highest attenuating material in the sample. It should be noted that another scaling would yield different results, especially for the high-attenuating structure Ni_3Sn_2 which has an attenuation coefficient close to Ni_3Sn_4. Additionally, the simulations would be more reliable in analyzing the different phases in the measured reconstructed sample if the simulations could account for the phase information that has been observed in the ESRF measurements.

Chapter 6

Conclusion

In this thesis we have presented a two-dimensional parallel beam geometry CT simulation software that has been optimized to replicate a Nikon XT H 225 ST CT instrument. The optimization consisted of determining an adjustable parameter $\eta(V)$, the measured photon flux $N(V, I)$ and the focal spot size $\sigma(P)$. The parameter $\eta(V)$ was introduced due to observed differences between the X-ray transmission in measured and simulated projections, and it was demonstrated that the parameter $\eta(V)$ had a non-linear dependence on the tube voltage.

The measured photon flux had to be determined in order to apply Poisson noise to the projections. The results indicated a linear relationship between the measured photon flux and the tube voltage. With the measured photon flux, the simulated projections with noise were found to replicate the experimental projections well.

Estimates of the focal spot size were acquired assuming that the focal spot could be modeled as a Gaussian distribution. Results were obtained for powers ranging from 10 to 30 W. The results indicated a linear relationship between the Full Width at Half Maximum of the focal spot size and the power setting, starting at 29.3 μm at 7 W and increasing with 0.28 μm/W. These results differ from information provided by Nikon, who guarantees a focal spot size of 3 μm at 7 W increasing approximately with 1 μm/W. It is thought that the discrepancy is largely due to differences between the assumed Gaussian model and the real focal spot distribution.

Polychromatic CT simulations of three homogeneous, cylindrical samples consisting of POM, Teflon and Al, respectively, were compared to experimentally measured tomograms. It was demonstrated that the noise in the simulated tomograms fit the experimental data well. The POM simulation gave more noise than the measured sample, while the simulated Al and Teflon samples gave more beam hardening than the measured tomograms.

Polychromatic CT simulations of the sample containing two Si layers bonded by Ni and Ni_3Sn_2

demonstrated the effects that a finite focal spot size has on the physical resolution in tomograms. It was shown that both the reconstruction algorithm and the focal spot size influence the resolution in the reconstructed tomograms. Using a current of 100 μA and a pixel size of 4 μm, the thinnest resolvable Ni_3Sn_2 layer was found to be 64 μm. Moreover, the tomograms were affected by beam hardening, having a relative error between the edge and the center value in the Ni_3Sn_2 center profile of 18 %. It was shown that the relative error could be reduced to 12 % by changing the filter from a 1.00 mm Cu filter to a 1.00 mm Ag filter at the expense of increased noise. Finally, reducing the current from 100 μA to 10 μA showed that the thinnest resolvable Ni_3Sn_2 layer was 56 μm. The thinnest resolvable layer presented here most likely differs from the actual CT instrument as the measured focal spot size is far larger than the real size. A comparison with a focal spot size of 3 μm as guaranteed by Nikon, revealed that the physical resolution should not be worse than 16 μm for a pixel size of 4 μm and that the physical resolution is not affected by the focal spot size.

The Au-Sn SLID sample was measured and reconstructed with a voxel size of 3.69 μm^3. The sample showed presence of the cupping artifact in the PZT and WC part of the sample. Moreover, varying attenuation values along the vertical direction were observed. Two additional measurements indicated that the attenuation variations were due to the CT system and not the sample itself. It was argued that the variations were due to the anode heel effect.

Finally, it was demonstrated that the Ni-Sn SLID sample measured at ESRF was composed of primarily two structures in the bond layer, a highly attenuating structure and a weakly attenuating structure. Comparing simulations with the measured data indicated that the weak attenuating structure consisted of Ni. Moreover, it was argued that the Ni structure was partially filled with voids with sizes similar to or smaller than the voxel size. It was also demonstrated that the high attenuating structure could consist of Ni_3Sn_2, however, other phases could also be present in this structure as the range of attenuation values in the structure was large. Lastly, it was argued that the results obtained through simulations could be improved if the simulations could account for the phase contrast as well.

6.1 Future work

Although the current implementation of the CT simulations shows good agreement between simulated and measured tomograms, there are several improvements that can be done. The necessity of the parameter $\eta(V)$ indicates that parts of the CT instrument have not been accurately modeled. If there are discrepancies between the simulated and real source spectra, transmission deviations must be expected. The simulated spectrum should be verified by measuring the real spectrum and comparing it to the simulated spectrum. Moreover, the thickness of the Al protection layer in front of the detector is proprietary information of the X-ray detector manufacturer. It is believed that the parameter could be partially or completely removed if this was corrected. As this would also

reduce the discrepancy between the simulated and measured projected X-ray transmissions, the estimated photon flux should also improve.

Two simplifications have been used in the simulations. First, scattering has been treated as an absorption. For Rayleigh scattering, which scatters the photons only slightly, the scattered photons may be redistributed on the X-ray detector. Although Compton scattered photons are scattered over a larger angle than the Rayleigh scattering, parts of the Compton scattered photons may also hit the X-ray detector. Second, the simulations were simplified by assuming a parallel beam profile instead of the cone beam geometry. Although this is considered to be a minor issue, deviations between simulated and measured projections should be expected farther from the direct beam axis and towards the boundary of the X-ray detector. By correctly modelling the physics of scattering and introducing either a fanbeam geometry or a fully three dimensional cone-beam geometry, improvements of the simulations should be expected.

Finally, the simulations of the Ni-Sn SLID sample indicated which phases could be observed in the reconstructed sample. However, without a proper treatment of the phase-contrast, the results remain partially speculative. By implementing a full treatment of the phase-propagation as well, the potential to use simulations to analyze measured, reconstructed tomograms using a monochromatic and partially coherent source should be more viable.

Bibliography

[1] A. C. Kak, M. Slaney, and G. Wang. *Principles of Computerized Tomographic Imaging*, volume 29. American Association of Physicists in Medicine, January 2002.

[2] M. Paziresh, A. M. Kingston, S. J. Latham, W. K. Fullagar, and G. M. Myers. Tomography of atomic number and density of materials using dual-energy imaging and the Alvarez and Macovski attenuation model. *Journal of Applied Physics*, 119(21), June 2016.

[3] L. Salvo, P. Cloetens, E. Maire, S. Zabler, J. J. Blandin, J. Y. Buffiere, W. Ludwig, E. Boller, D. Bellet, and C. Josserond. X-ray micro-tomography an attractive characterisation technique in materials science. *Nuclear Instruments & Methods In Physics Research Section B-Beam Interactio*, 200:273–286, January 2003.

[4] D. A. Coucheron, M. Fokine, N. Patil, D. W. Breiby, O. T. Buset, N. Healy, A. C. Peacock, T. Hawkins, M. Jones, J. Ballato, and U. J. Gibson. Laser recrystallization and inscription of compositional microstructures in crystalline SiGe-core fibres. *Nature Communications*, 7, October 2016.

[5] J. F. Barrett and N. Keat. Artifacts in ct: Recognition and avoidance. *RadioGraphics*, 24(6):1679–1691, 2004. PMID: 15537976.

[6] R. Schulze, U. Heil, D. Groß, D.D. Bruellmann, E. Dranischnikow, U. Schwanecke, and E. Schoemer. Artefacts in cbct: A review. *Dentomaxillofacial Radiology*, 40(5):265–273, July 2011.

[7] R. E. Alvarez and A. Macovski. Energy-selective reconstructions in X-ray computerized tomography. *Physics in medicine and biology*, 21(5), September 1976.

[8] B. J. Heismann, J. Leppert, and K. Stierstorfer. Density and atomic number measurements with spectral x-ray attenuation method. *Journal of Applied Physics*, 94(3):2073–2079, August 2003.

[9] K. Achterhold, M. Bech, S. Schleede, G. Potdevin, R. Ruth, R. Loewen, and F. Pfeiffer. Monochromatic computed tomography with a compact laser-driven x-ray source. *Scientific Reports*, 3(1), February 2013.

[10] P. Duvauchelle, N. Freud, V. Kaftandjian, and D. Babot. A computer code to simulate x-ray imaging techniques. *Nuclear Inst. and Methods in Physics Research, B*, 170(1):245–258, 2000.

[11] I. Kawrakow, E. Mainegra-Hing, D. W. O. Rogers, F. Tessier, and B. R. B. Walters. The EGSnrc code system: Monte Carlo simulation of electron and photon transport. Technical Report PIRS-701, National Research Council Canada, 2017.

[12] K. M. Rosenberg. CTSim 3.5 User Manual. Heart hospital of New Mexico, Albuquerque.

[13] A Larsson, T. A. Tollefsen, and K. E. Aasmundtveit. Ni-sn solid liquid interdiffusion (slid) bonding - process, bond characteristics and strength. In *2016 6th Electronic System-Integration Technology Conference (ESTC)*, 2016.

[14] T. Tollefsen, A. Larsson, M. Taklo, A. Neels, X. Maeder, K. Høydalsvik, D. Breiby, and K. Aasmundtveit. Au-sn slid bonding: A reliable ht interconnect and die attach technology. *Metallurgical and Materials Transactions*, 44(2):406–413, April 2013.

[15] D. Paganin, S. C. Mayo, T. E. Gureyev, P. R. Miller, and S. W. Wilkins. Simultaneous phase and amplitude extraction from a single defocused image of a homogeneous object. *Journal Of Microscopy-Oxford*, 206:33–40, April 2002.

[16] F. H. Attix. *Introduction to Radiological Physics and Radiation Dosimetry*. Wiley, 1986.

[17] J.H. Hubbell and S.M. Seltzer. Tables of X-Ray Mass Attenuation Coefficients and Mass Energy-Absorption Coefficients (version 1.4). Available: http://physics.nist.gov/xaamdi [2017, December]. National Institute of Standards and Technology, Gaithersburg, MD.

[18] J. Als-Nielsen. *Elements of modern X-ray physics*. Wiley, Chichester, 2nd ed. edition, 2011.

[19] J. M. Boone, T. R. Fewell, and R. J. Jennings. Molybdenum, rhodium, and tungsten anode spectral models using interpolating polynomials with application to mammography. *Medical Physics*, 24(12):1863–1874, December 1997.

[20] J. M. Boone and J. A. Seibert. An accurate method for computer-generating tungsten anode x-ray spectra from 30 to 140 kv. *Medical Physics*, 24(11):1661–1670, November 1997.

[21] G. G. Poludniowski and P. M. Evans. Calculation of x-ray spectra emerging from an x-ray tube. part i. electron penetration characteristics in x-ray targets. *Medical Physics*, 34(6), 2007.

[22] H. K. Kim, I. A. Cunningham, Z. Yin, and G. Cho. On the development of digital radiography detectors: A review. *International Journal of Precision Engineering and Manufacturing*, 9:86–100, 10 2008.

[23] C. W. E. van Eijk. Inorganic scintillators in medical imaging. *Physics in Medicine and Biology*, 47(8):R85–R106, April 2002.

[24] S. N. Ahmed. *Physics and Engineering of Radiation Detection*. Elsevier Science, 2 edition, November 2014.

[25] P. Lecoq. *Inorganic scintillators for detector systems*. Particle Acceleration and Detection. 2nd ed. 2017. edition, 2017.

[26] A. Kueh, J. M. Warnett, G. J. Gibbons, J. Brettschneider, T. E. Nichols, M. A. Williams, and W. S. Kendall. Modelling the penumbra in Computed Tomography. *Journal of X-ray science and technology*, 24(4), 21 2016.

[27] S. Kam S. H. Kim J. W. Park H. Jeon H. Youn, H. K. Kim. Physics-based modeling of computed tomography systems, 2015.

[28] M. Salamon, R. Hanke, P. Krüger, F. Sukowski, N. Uhlmann, and V. Voland. Comparison of different methods for determining the size of a focal spot of microfocus x-ray tubes. *Nuclear Inst. and Methods in Physics Research, A*, 591(1):54–58, 2008.

[29] B. R. Whiting, P. Massoumzadeh, O. A. Earl, J. A. O'Sullivan, D. L. Snyder, and J. F. Williamson. Properties of preprocessed sinogram data in x-ray computed tomography. *Medical Physics*, 33(9), 2006.

[30] T. Weitkamp, D. Haas, D. Wegrzynek, and A. Rack. ANKAphase: software for single-distance phase retrieval from inline x-ray phase-contrast radiographs. *Journal of synchrotron radiation*, 18(Pt 4), July 2011.

[31] M A Beltran, D M Paganin, K Uesugi, and M J Kitchen. 2d and 3d x-ray phase retrieval of multi-material objects using a single defocus distance. *Optics express*, 18(7), March 2010.

[32] R. A. Street. *Technology and Applications of Amorphous Silicon*, volume 37 of *Springer Series in Materials Science*. Springer, 2000.

[33] J. H. Siewerdsen, L. E. Antonuk, Y. El-Mohri, J. Yorkston, W. Huang, and I. A. Cunningham. Signal, noise power spectrum, and detective quantum efficiency of indirect-detection flat-panel imagers for diagnostic radiology. *Medical Physics*, 25(5):614–628, May 1998.

[34] L. W. Goldman. Principles of ct: Radiation dose and image quality. *Journal of Nuclear Medicine Technology*, 35(4):213–225, December 2007.

[35] S. Mori, M. Endo, K. Nishizawa, M. Ohno, H. Miyazaki, K. Tsujita, and Y. Saito. Prototype heel effect compensation filter for cone-beam ct. *Physics in Medicine and Biology*, 50(22):N359–N370, November 2005.

[36] A. D. Oliveira, M. J. Fartaria, J. Cardoso, L. M. Santos, C. Oliveira, M. F. Pereira, and J. G. Alves. The determination of the focal spot size of an X-ray tube from the radiation beam profile. *Radiation Measurements*, 82:138–145, November 2015.

[37] R. B. Benítez, R. Ning, D. Conover, and S. Liu. Nps characterization and evaluation of a cone beam ct breast imaging system. *Journal of X-Ray Science and Technology*, 17(1):17–40, 2009.

[38] A. Thompson, D. Attwood, E. Gullikson, M. Howells, K. Kim, J. Kirz, J. Kortright, I. Lindau, P. Liu, Y. Pianetta, A. Robinson, J. Scofield, J. Underwood, G. Williams, and H. Winick. X-ray data booklet. http://xdb.lbl.gov/xdb-new.pdf, 2009. 2nd edition, Lawrence Berkeley National Laboratory.

[39] M. D. S. W. Yoon, K. Glover, and K. Shiozaki. Nickel-Tin Transient Liquid Phase Bonding Toward High-Temperature Operational Power Electronics in Electrified Vehicles. *Power Electronics, IEEE Transactions on*, 28(5):2448–2456, May 2013.

[40] Springer Materials: Alloy densities. http://materials.springer.com/periodictable#. Accessed: December 2017.

[41] W. Gautschi. *Numerical analysis*. Birkhauser, Boston, 2nd ed. edition, 2012.

[42] J. Hiller, M. Maisl, and L. M. Reindl. Physical characterization and performance evaluation of an x-ray micro-computed tomography system for dimensional metrology applications. *Measurement Science and Technology*, 23(8), August 2012.